number) were surrogated as an index and chronologically compared between HAP1/ataxin-3Q27 and HAP1/ataxin-3Q79-cotransfected cells. The HA3-CAF ratios for ataxin-3Q27 and ataxin-3Q79 (HA3Q27-CAF and HA3Q79-CAF ratios) were approximately 33.7 and 34.8% in 24 h and 34.1 and 36.1% in 48 h after each cotransfection (Fig. 3g). There was no significant difference between HA3Q27-CAF and HA3Q79-CAF ratios. Coimmunoprecipitation tests were carried out to obtain biochemical evidence for the interaction of HAP1 with ataxin-3Q27 or ataxin-3Q79 (Fig. 3h–j).

Fig. 3

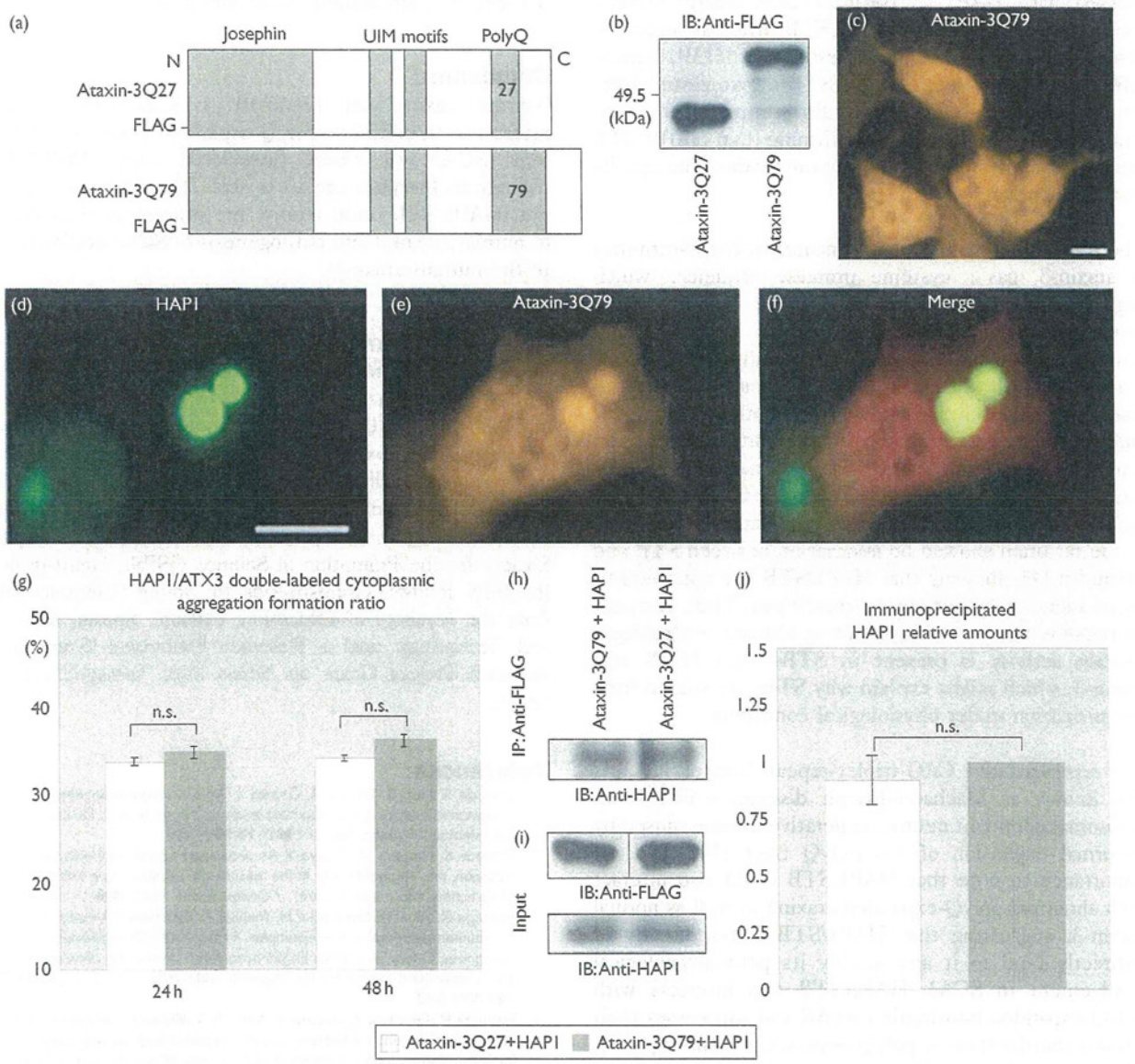

Interaction of huntingtin-associated protein 1 (HAP1)/stigmoid body with polyQ-expanded ataxin-3. (a) Diagrams of the primary structures of ataxin-3Q27 and ataxin-3Q79. (b) Western blot for extracts from ataxin-3Q27-transfected and ataxin-3Q79-transfected cells. (c) Fluorescence immunocytochemistry for ataxin-3Q79-transfected cells. (d–f) Fluorescence photomicrographs showing subcellular expression of HAP1 and ataxin-3Q79. Note that merged images show colocalization of HAP1 and ataxin-3Q79 (f) (bars = 10 μm). (g) Bar graph comparing HAP1/ataxin-3 double-labeled cytoplasmic aggregation formation ratios between ataxin-3Q27 and ataxin-3Q79 in time course (24 and 48 h) after the cotransfection into cells (ns, not significant). (h and i) Coimmunoprecipitation analysis of protein lysates from HAP1/ataxin-3Q27-cotransfected and HAP1/ataxin-3Q79-cotransfected cells. Inputs are the control of proteins exogenously expressed. (j) Quantification of the each immunoprecipitated HAP1 protein normalized to ataxin-3Q27 and ataxin-3Q79.

In cells coexpressing HAP1 and ataxin-3Q27, or ataxin-3Q79, HAP1 was coprecipitated. There was no significant difference in immunoprecipitated HAP1 relative amounts between ataxin-3Q27 and ataxin-3Q79.

Discussion

In this study, the most striking finding is that HAP1/STB are closely associated with normal ataxin-3Q27 and mutant ataxin-3Q79 derived from a SCA3 patient. Furthermore, even the Josephin domain alone coexpressed with HAP1 in Neuro2a cells clearly showed intimate association with HAP1/STB, whereas Josephin-deleted mutant ataxin-3 coexpressed with HAP1 turned diffuse and irrelevant to HAP1/STB in cytoplasm. Data for immunoprecipitation assay also supported the immunocytochemical results, confirming that HAP1/STB can interact with normal and mutant ataxin-3 through its Josephin domain.

The Josephin domain, which is located at the *N*-terminus of ataxin-3, has a cysteine protease sequence, which suggests potential ubiquitin protease activity [15]. Josephin domain also represses histone acetylation and transcription by binding to histone and transcriptional coactivator [16]. As HAP1/STB is intracellularly associated with ataxin-3 through its Josephin domain, it might partially modify the function of the putative ubiquitin protease or transcriptional repressor of ataxin-3. Interestingly, ataxin-3 was reported to be a typical deubiquitinating enzyme [17]. Our earlier immunohistochemical study in the rat brain showed no association between STB and ubiquitin [4], showing that HAP1/STB is a nonubiquitinated inclusion under normal conditions. Thus, it might be possible that a deubiquitinating enzyme or deubiquitination activity is present in STBs with HAP1 and ataxin-3, which might explain why STBs are spared from ubiquitination under physiological conditions.

The representative CAG-triplet-repeat disease, SCA3, is also known as Machado–Joseph disease, which is an autosomal dominant neurodegenerative disease caused by abnormal expansion of the polyQ tract [14]. It is of importance to note that HAP1/STB could also interact with abnormal polyQ-expanded ataxin3 as well as normal ataxin-3, suggesting that HAP1/STB could directly or indirectly bind to it and modify its pathophysiological involvement in SCA3. HAP1/STB also interacts with polyQ-expanded huntingtin and AR and suppresses their nuclear translocation in polyQ-dependent manner [9,10]. Thus, it could more efficiently neutralize the toxicity of the polyQ-expanded mutant forms in pathogenesis of Huntington's disease and SBMA and protect against the cell death. In SCA17 and Joubert syndrome, the affinities of HAP1/STB with pathological mutants of TATA-binding protein and Abelson helper integration site 1 are less strong than normal forms [11,12]. Nevertheless, HAP1/STB could serve as a cytoplasmic neuroprotective component interfering with 'gain-of-toxic function' of their pathological mutants [11,12]. HAP1/STB expression might raise the threshold of vulnerability for cell death and render more beneficial stability to cells with HAP1/STB than without it, as the 'HAP1/STB protection hypothesis' predicts [7]. Thus, in this study, although HAP1/STB seems to interact with ataxin-3 in polyQ-independent manner, it might be possible that HAP1/STB plays an important role in modification on physiological functions of normal ataxin-3 and on SCA3 pathogenesis attributable to ataxin-3Q79.

Conclusion

Normal ataxin-3 was identified as a new HAP1/STB interactor. In addition, polyQ-expanded ataxin-3 derived from SCA3 was closely associated with HAP1/STB through its Josephin domain as well. The findings suggest that HAP1/STB could modify the physiological function of normal ataxin-3 and pathogenesis of SCA3 attributable to the mutant ataxin-3.

Acknowledgements

We are grateful to Ms. Yurika Koto, Ms. Risa Andachi, Mr. Chikahisa Matsuo, Mr. Jun Oba, Ms. Yumiko Matsuzaki, and Ms. Miyuki Takeshita for technical assistance in the early stages of this study. We also acknowledge the technical expertise of the DNA Core facility of the Center for Gene Research, Yamaguchi University. This study was supported by Grant-in-Aid for Scientific Research (C) from the Japan Society for the Promotion of Science (JSPS), Grant-in-Aid for JSPS fellows, Grant-in-Aids for Young Scientists (B) from the Ministry of Education, Culture, Sports, Science and Technology, and a Research Promotion Grant and Research Project Grant on Stress from Yamaguchi University.

References

1 Shinoda K, Mori S, Ohtsuki T, Osawa Y. An aromatase-associated cytoplasmic inclusion, the 'stigmoid body,' in the rat brain: I. Distribution in the forebrain. *J Comp Neurol* 1992; **15**:360–376.
2 Shinoda K, Nagano M, Osawa Y. An aromatase-associated cytoplasmic inclusion, the 'stigmoid body,' in the rat brain: II. Ultrastructure (with a review of its history and nomenclature). *J Comp Neurol* 1992; **329**:1–19.
3 Fujinaga R, Yanai A, Nakatsuka H, Yoshida K, Takeshita Y, Uozumi K, *et al.* Anti-human placental antigen complex X-P2 (hPAX-P2) anti-serum recognizes C-terminus of huntingtin-associated protein 1A common to 1B as a determinant marker for the stigmoid body. *Histochem Cell Biol* 2007; **128**:335–348.
4 Fujinaga R, Takeshita Y, Uozuimi K, Yanai A, Yoshioka K, Kokubu K, *et al.* Microtubule-dependent formation of the stigmoid body as a cytoplasmic inclusion distinct from pathological aggresomes. *Histochem Cell Biol* 2009; **132**:305–318.
5 Li SH, Gutekunst CA, Hersch SM, Li XJ. Association of HAP1 isoforms with a unique cytoplasmic structure. *J Neurochem* 1998; **71**:2178–2185.
6 Gutekunst CA, Li SH, Yi H, Ferrante RJ, Li XJ, Hersch SM. The cellular and subcellular localization of huntingtin-associated protein 1 (HAP1): comparison with huntingtin in rat and human. *J Neurosci* 1998; **18**:7674–7686.
7 Fujinaga R, Kawano J, Matsuzaki Y, Kamei K, Yanai A, Sheng Z, *et al.* Neuroanatomical distribution of huntingtin-associated protein 1-mRNA in the male mouse brain. *J Comp Neurol* 2004; **478**:88–109.

8 Li SH, Yu ZX, Li CL, Nguyen HP, Zhou XY, Deng C, *et al.* Lack of huntingtin-associated protein-1 causes neuronal death resembling hypothalamic degeneration in Huntington's disease. *J Neurosci* 2003; **23**:6956–6964.

9 Li XJ, Li SH, Sharp AH, Nucifora FC Jr, Schilling G, Lanahan A, *et al.* A huntingtin-associated protein enriched in brain with implications for pathology. *Nature* 1995; **378**:398–402.

10 Takeshita Y, Fujinaga R, Zhao C, Yanai A, Shinoda K. Huntingtin-associated protein 1 (HAP1) interacts with androgen receptor (AR) and suppresses SBMA-mutant-AR-induced apoptosis. *Hum Mol Genet* 2006; **15**:2298–2312.

11 Prigge JR, Schmidt EE. HAP1 can sequester a subset of TBP in cytoplasmic inclusions via specific interaction with the conserved TBP(CORE). *BMC Mol Biol* 2007; **8**:76.

12 Sheng G, Xu X, Lin FY, Wang CE, Rong J, Cheng D, *et al.* Huntingtin-associated protein 1 interacts with Ahi1 to regulate cerebellar and brainstem development in mice. *J Clin Invest* 2008; **118**:2785–2795.

13 Tori F, Akelai A, Lupoli S, Siromi M, Amann-Zaicenstein D, Fumagalli MA, *et al.* Fine mapping of AHI1 as a schizophrenia susceptibility gene: from association to evolutionary evidence. *FASEB J* 2010; **24**: 3066–3082.

14 Kawaguchi Y, Okamoto T, Taniwaki M, Aizawa M, Inoue M, Katayama S, *et al.* CAG expansions in a novel gene for Machado-Joseph disease at chromosome 14q32.1. *Nat Genet* 1994; **8**:221–228.

15 Doss-Pepe EW, Stenroos ES, Johnson WG, Madura K. Ataxin-3 interactions with Rad3 and valosin-containing protein and its associations with ubiquitin chains and the proteasome are consistent with a role in ubiquitin-mediated proteolysis. *Mol Cell Biol* 2003; **23**:6469–6483.

16 Li F, MacFarlan T, Pittman RN, Chakravarti D. Ataxin-3 is a histone-binding protein with two independent transcriptional corepressor. *J Biol Chem* 2002; **277**:45004–45012.

17 Burnett B, Li F, Pittman RN. The polyglutamine neurodegenerative protein ataxin-3 binds polyubiquitylated proteins and has ubiquitin protease activity. *Hum Mol Genet* 2003; **12**:3195–3205.

Longitudinal and Simultaneous Imaging of Retinal Ganglion Cells and Inner Retinal Layers in a Mouse Model of Glaucoma Induced by *N*-Methyl-D-Aspartate

Noriko Nakano,[1] *Hanako Ohashi Ikeda,*[1] *Masanori Hangai,*[1] *Yuki Muraoka,*[1] *Yoshinobu Toda,*[2] *Akira Kakizuka,*[3] *and Nagahisa Yoshimura*[1]

Purpose. To investigate the longitudinal profile of *N*-methyl-D-aspartate (NMDA) injection–induced damage in retinal ganglion cells (RGCs) by imaging retinal Thy 1-cyan fluorescent protein (CFP) expression and inner retinal layers using a custom-made imaging device containing short-wavelength confocal scanning laser ophthalmoscope (scSLO) and speckle noise-reduced spectral-domain optical coherence tomography (SD-OCT).

Methods. Simultaneous scSLO and SD-OCT examinations were performed in Thy 1-CFP mice injected with NMDA (1–20 nanomoles). CFP-expressing RGCs were counted using scSLO images. Ganglion cell complex (GCC: retinal nerve fiber layer, ganglion cell layer, and inner plexiform layer) thickness around the optic disc was measured in SD-OCT images.

Results. The RGCs rapidly decreased 1 day after NMDA injection in a dose-dependent manner (65.3%, 71.7%, 49.5%, and 27.1% of the preinjection level, 2, 5, 10, and 20 nanomoles, respectively) and continued to decrease slightly (to 53.7%, 44.1%, 28.3%, and 20.2% of the preinjection level on days 14, 2, 5, 10, and 20 nanomoles, respectively). In contrast, dose-dependent reduction of GCC thickness was first detected 4 days after injection. The thickness further decreased to 84.6%, 75.7%, 76.5%, and 71.4% of the preinjection level on day 14 (2, 5, 10, and 20 nanomoles, respectively).

Conclusions. NMDA-induced RGC damage is characterized by rapid RGCs loss followed by gradual reduction in GCC thickness. Simultaneous imaging of CFP expression in the RGCs and inner retinal layers provides a sensitive, reliable, and new method for longitudinal evaluation of progressive RGC damage in experimental models of glaucoma. (*Invest Ophthalmol Vis Sci.* 2011;52:8754–8762) DOI:10.1167/iovs.10-6654

Glaucoma, the second leading cause of vision loss in the world,[1] is caused by progressive retinal ganglion cell (RGC) loss due to damage to the RGC axon within the optic nerve head[2] and damage to the soma of the RGC. Currently, several noninvasive methods for in vivo experimental assessment of progressive RGC loss have been performed, using high-end optical imaging technologies including optical coherence tomography (OCT) and confocal scanning laser ophthalmoscopy (cSLO), which provide a unique opportunity to study RGC injury longitudinally without euthanizing animals at multiple time points.[3–12]

OCT is an interferometric imaging technology and enables high-resolution, cross-sectional imaging of fundus structures in vivo. It has been clinically used in glaucoma patients to help diagnosis of the disease or to monitor disease progression. For example, circumpapillary retinal nerve fiber layer (cpRNFL) thickness or macular ganglion cell complex (GCC) thickness, which includes the RNFL, ganglion cell layer (GCL), and inner plexiform layer (IPL) has been shown to be useful and reliable to diagnose or to assess the disease. In experimental glaucoma models, OCT also allows investigators to monitor changes in the thickness of the whole retina and the retinal nerve fiber layer (RNFL) in rodents.[5,10–12] In contrast with originally developed time-domain OCT (TD-OCT), recently developed spectral-domain OCT (SD-OCT) technology improves visualization of the individual retinal layers, such as GCL and IPL, by speckle noise reduction, which is the most influential artificial noise that blurs the boundaries of the retinal layers.[13] Especially, SD-OCT with a three-dimensional eye-tracking system enables obtaining multiple B-scans at an identical location of interest. Exact averaging of B-scans results in a sufficient reduction in speckle noise to greatly improve visualization of RGC-related inner retinal layer boundaries.[12,14] The technique would enable more reliable assessment of the decreasing thickness of the individual inner retinal layers and RGC-related complex as RGC injuries progress in glaucoma patients[15–18] and in rodents models of glaucoma.[12]

On the other hand, cSLO enables investigators to directly monitor individual RGCs that are labeled genetically[6,7,9] or by retrograde labeling[4] and apoptotic RGCs that are labeled fluorescently with annexin 5 (DARC).[3] Because RGC imaging at the cellular level is not feasible in living human eyes, the RGC imaging methods using cSLO in experimental animals provide unique advantages for investigating the pathogenesis of RGC death. Moreover, counting the number of RGCs on cSLO images of identical eyes at multiple time points facilitates assessment of the neuroprotective effects of drugs or chemicals on RGCs in vivo. The thickness of the inner retinal layer and the number of RGCs are associated with RGC damage in the same

From the [1]Department of Ophthalmology and Visual Sciences and the [2]Center for Anatomical Studies, Kyoto University Graduate School of Medicine, Kyoto, Japan; and the [3]Laboratory of Functional Biology, Kyoto University Graduate School of Biostudies and Solution Oriented Research for Science and Technology, Kyoto, Japan.

Presented at the annual meeting of the Association for Research in Vision and Ophthalmology, Fort Lauderdale, Florida, May 2010.

Supported in part by the Innovative Techno-Hub for Integrated Medical Bio-imaging Project of the Special Coordination Funds for Promoting Science and Technology; Grant-in-Aid for Young Scientists 22791656 from the Ministry of Education, Culture, Sports, Science and Technology (MEXT); and a research grant from the Astellas Foundation for Research on Metabolic Disorders.

Submitted for publication September 29, 2010; revised January 31, May 31, and September 1, 2011; accepted October 9, 2011.

Disclosure: **N. Nakano**, None; **H.O. Ikeda**, None; **M. Hangai**, None; **Y. Muraoka**, None; **Y. Toda**, None; **A. Kakizuka**, None; **N. Yoshimura**, None

Corresponding author: Hanako Ohashi Ikeda, Department of Ophthalmology and Visual Sciences, Kyoto University Graduate School of Medicine, 54 Kawahara-cho, Shogoin, Sakyo-ku, Kyoto 606-8507, Japan; hanakoi@kuhp.kyoto-u.ac.jp.

Investigative Ophthalmology & Visual Science, November 2011, Vol. 52, No. 12

experimental setting using identical animals. However, no previous studies have monitored these two distinct but mutually related parameters simultaneously.

To reveal the relationship between RGC damage at the cellular level and retinal thickness related to the RGCs, we developed a custom-made imaging system for animals based on a commercial system (Spectralis HRA+OCT; Heidelberg Engineering, Heidelberg, Germany). The combined system contains a cSLO, a custom-made short-wavelength confocal scanning laser ophthalmoscope (scSLO), and an SD-OCT system with an eye-tracking function. In addition to a laser for detecting fluorescein protein (488 nm), the instrument includes a laser with a short wavelength (445 nm) that is optimized for detecting cyan fluorescent protein (CFP; major excitation peak, 433 nm; major emission peak, 475 nm).[19] This approach enables detection of individual RGCs in Thy 1-CFP transgenic mice,[20] in which CFP expression is controlled by the *Thy 1* promoter. Thy 1 is a cell-surface glycoprotein expressed by projection neurons in many parts of the nervous system[21]; in the retina, it is most exclusively expressed in RGCs.[22]

N-methyl-D-aspartate (NMDA)-induced excitotoxicity is a well-known model to induce RGC injury.[23] In the retina, RGCs and a subset of cells in the inner nuclear layer (INL) express subunits of NMDA receptor. RGCs are exquisitely sensitive to the effects of glutamate and the glutamate analog NMDA, which causes dose-dependent loss of RGCs.[23,24] NMDA-induced excitotoxicity, as well as neurotrophin deprivation induced by optic nerve crush or transection, has been implicated in the pathogenesis of glaucoma and widely used as a glaucoma model.[25,26]

The purpose of this study was to determine the feasibility of longitudinal monitoring of RGC damage, on both individual cell imaging and measurement of the thickness of inner retinal layers using combined scSLO and speckle noise-reduced SD-OCT. Using intravitreal NMDA injection to induce RGC injury, we assessed the profile of progressive RGC degeneration from the dual aspects of the number of CFP-expressing RGCs and the thickness of the ganglion cell complex (GCC), which includes RNFL, RGC, and IPL in Thy 1-CFP transgenic mice.

Methods

Combined Imaging System of scSLO and Speckle Noise–Reduced SD-OCT with an Eye-Tracking Function

An imaging system that combines scSLO and speckle noise-reduced SD-OCT with an eye-tracking function was customized (based on a Spectralis HRA+OCT), to modify the SLO system to an optimal wavelength of light source for CFP imaging (termed the Multiline OCT system) by Heidelberg Engineering (Heidelberg, Germany). This system includes a short-wavelength (445 nm) diode laser and a barrier filter with a 488-nm cutoff to visualize the CFP protein. The scan rate of the scSLO is 12 frames per second, with a digital resolution of 512 × 512 pixels in each frame. The OCT instrument uses an 870-nm superluminescent diode as a light source. The scan rate of the SD-OCT is 47,000 A-scans per second, with an axial resolution of ~7 μm. The simultaneous SLO and SD-OCT imaging of the retina enables real-time three-dimensional tracking of eye movements, which allows precise real-time averaging of multiple SLO and B-scan images acquired at each identical location of interest on the retina to reduce speckle noise.[14]

Experimental Animals

All studies were conducted in compliance with the ARVO Statement for the Use of Animals in Ophthalmic and Vision Research. Transgenic mice, B6.Cg-Tg (Thy 1-CFP) 23Jrs/J, in which CFP is expressed under the *Thy 1* promoter were obtained from the Jackson Laboratory (Bar Harbor, ME). Genotyping was performed with the PCR method, as instructed. The environment was maintained in 12-hour light–dark cycle. All the mice were fed ad libitum. Male mice (age, 8–10 weeks; weight, 25–30 g) were used in the experiments. Before image acquisition or intravitreal injection, the mice were anesthetized by an intraperitoneal injection of pentobarbital (50 mg/kg body weight). Pupils were dilated to approximately 2 mm in diameter with tropicamide and phenylephrine (0.5% each) eye drops.

Mouse Acute RGC Injury Model Mediated by NMDA

NMDA (20 nanomoles/2 μL [n = 15], 10 nanomoles/2 μL [n = 15], 5 nanomoles/2 μL [n = 10], 2 nanomoles/2 μL [n = 10], and 1 nanomoles/2 μL [n = 6]) was injected into the vitreous of the eyes of Thy 1-CFP mice using a 33-gauge needle (Ito Corporation, Shizuoka, Japan). Control mice (n = 15) were injected with the same volume of phosphate-buffered saline (PBS).

Image Acquisition

scSLO and SD-OCT examinations were performed simultaneously at 1, 2, 4, 7, and 14 days after the injection. For fundus imaging, PMMA contact lenses optimal for mice (Heidelberg Engineering) were placed on the corneas. Use of the lenses prevents anesthesia-induced cataract progression. A 25-D adaptor lens was placed on the objective lens of the Multiline OCT to focus on the mouse retina. For imaging of the inner retinal layers on SD-OCT using the speckle noise-reduction method, six radial B-scans through the optic disc and a circular scan around the optic disc were performed. In this study, the maximum number of B-scans set by the manufacturer (100 for line scans and 16 for circular scans) were used for averaging. For RGC imaging on scSLO, we averaged 30 scSLO images per scan area.

Manual Measurement of GCC Thickness

The software used for drawing boundary lines was based on the built-in Spectralis HRA+OCT and provided by Heidelberg Engineering software to facilitate manual assessment of the B-scan images. This custom-made software allows various boundary lines to be drawn in each B-scan image. The software calculates the distance between the two manually drawn boundary lines for each layer of interest to yield a thickness value at each location. A boundary line was automatically placed along the border of the internal limiting membrane (ILM) and the vitreous, and another boundary line was manually placed between the inner plexiform layer (IPL) and INL in a masked fashion. The distance of these two lines was calculated as the GCC thickness.

With the optimal PMMA contact lens placed on the mouse cornea, the total focal length was 2.00 mm (in air). All lateral dimensions shown by the system software were originally scaled for a human eye, with a focal length of 16.447 mm (in air). This value was obtained using a modified Gullstrand eye and a gradient index lens provided by Heidelberg Engineering (Zinser G, personal communication, 2010). Therefore, to convert the lateral dimensions to those of the mouse eye, we multiplied the values (in millimeters) of the Spectralis by a factor of 2.00/16.447 = 0.122. In mouse eyes, the diameter of the circular scan with 12° (~3.4 mm in human eyes) was calculated as 0.420 mm, and the length of the15° line scan was 0.530 mm.

For GCC measurement along the radial scans, the mean GCC thickness (between 56–224 μm apart from the optic nerve head) along each scan was calculated by the software, and the mean GCC thickness of the six radial scans were averaged. The mean GCC thickness of a circular scan was also calculated by the software.

To assess the intradelineator and interdelineator reliability of the manual measurement of GCC thickness, two delineators (NN and AH) at the Kyoto University OCT Reading Center, who were masked to all experimental information drew the boundary lines for the measurement of GCC thickness on the circular SD-OCT scans. The boundary lines were drawn independently by the two delineators and redrawn on another day by one delineator (AH), as described previously.[27]

Counting of RGC

CFP-positive RGCs were manually counted within four 310-μm squares at a distance of 830 μm from the center of the optic nerve head on the scSLO images in a masked fashion. We selected the best images and determined the best areas in which the cells in the GCL were sharply focused. The number of counted RGCs from the four square areas were averaged.

Histologic Evaluation of Retinas

Immediately after image acquisition, we enucleated the eyeballs from the mice after a pentobarbital overdose. A suture was placed on the edge of the superior conjunctiva to identify the superior portion of the retina. The eyes were fixed in 4% paraformaldehyde for 24 hours at 4°C and embedded in paraffin. Serial 6-μm paraffin-embedded sections were cut through the suture and at the point of insertion of the optic nerve. The sections that passed through the center of the optic nerve head were selected. The selected retinal sections were stained with hematoxylin-eosin and photographed approximately 200 μm apart from the center of the optic disc under an optical microscope (Axioplan 2; Carl Zeiss GmbH, Jena, Germany). For each eye, GCC thickness of each retinal sections at 60, 100, and 200 μm from the optic nerve head (location matched with that at which GCC thickness was measured on radial SD-OCT scans) was measured with image-analysis software (Axio Vision 2.05; Carl Zeiss Vision GmbH), and the values were averaged. In some of these sections, we also counted the number of cells in GCL at days 0 and 1 (for each, $n = 3$).

Immunohistochemical staining was performed with antibodies to green fluorescent protein (GFP; rabbit, 1/500; MBL), syntaxin 1 (HPC-1; mouse, 1/100; Sigma-Aldrich), as a marker for amacrine cells, and Brn3 (goat, 1/50; Santa Cruz Biotechnology, Santa Cruz, CA), for RGC cells.[28] Nuclei were counterstained with a red fluorescent dye (TOTO-3; Invitrogen, Carlsbad, CA). Generally, procedures for fixing the paraffin-embedded sections break the native protein configuration without reducing the protein content, and this weakens the CFP fluorescent signals in the samples. We, therefore, used an anti-GFP antibody to detect the CFP-positive cells during immunohistochemical studies of paraffin-embedded sections. We used frozen sections (20 μm) for the detection of naïve CFP fluorescence and for staining with an anti-GFP antibody, because the fluorescence of CFP was faintly maintained in the frozen sections. The number of cells in the GCL that were positive or negative for each marker in the whole vertical sections (through the optic nerve head) of the retinas collected on days 0, 1, and 14 after NMDA injection (20 nanomoles, $n = 3$) was counted on images acquired with confocal microscopy (LSM 510; Carl Zeiss GmbH).

Statistical Analysis

A paired t-test was used to compare changes in the parameters before and after NMDA injection. Variables among mice injected with different dosage of NMDA were compared by analysis of variance and Scheffé's post hoc test. Linear regression analysis was used to correlate two parameters. The intraclass correlation coefficient (ICC) was calculated to test the intradelineator and interdelineator reliability of the manual measurement of GCC thickness on the circular scans (statistical analyses performed with PASW Statistics ver. 17.0; IBM SPSS, Chicago, IL). The level of statistical significance was set at $P < 0.05$.

Results

Retinal Imaging with Speckle Noise–Reduced SD-OCT Compared with Histologic Tissue Sections in Mice

With speckle noise reduction by averaging multiple B-scans, each layer of the retina, including the RNFL and GCL, in the mice was clearly visualized on the SD-OCT image, although the posterior boundary of the GCL was not as clear as the boundaries of the other layers (Fig. 1A). To test whether we could quantify inner retinal damage on the SD-OCT images, we injected 20 nanomoles of NMDA or PBS as a control into the vitreous of mouse eyes. In the histologic sections, 14 days after the injection, the number of ganglion cells was significantly reduced and the thicknesses of the RNFL, GCL, IPL, and GCC (including the RNFL, GCL, and IPL) were also significantly reduced in the injected eyes compared with the untreated or PBS-injected eyes (Fig. 1B). On the SD-OCT images, location matched with the histologic sections of identical eyes, and the anterior and posterior boundaries of the GCL became less clear

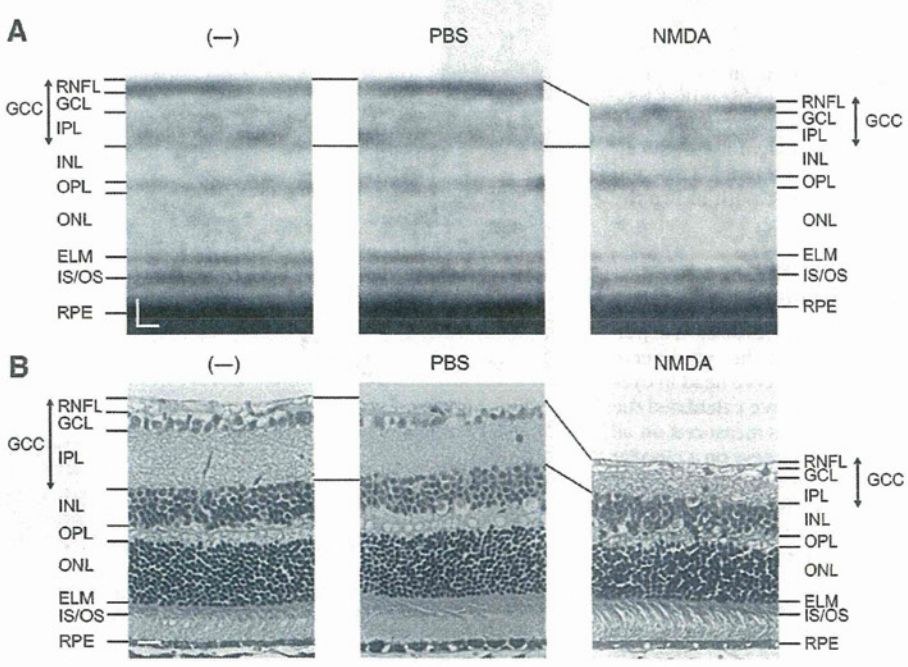

FIGURE 1. (A) Speckle noise–reduced SD-OCT images of mouse retinas. An untreated eye (*left*), an eye injected with PBS (*center*), and an eye injected with NMDA (20 nanomoles, *right*). All the images were location matched, 200 μm superior to the optic nerve head on a vertical scan through the center of the optic nerve head. (B) Retinal sections stained with HE at the retinal location corresponding to the SD-OCT images in (A). RNFL, retinal nerve fiber layer; GCL, ganglion cell layer; IPL, inner plexiform layer; GCC, ganglion cell complex; INL, inner nuclear layer; OPL, outer plexiform layer; ONL, outer nuclear layer; ELM, external limiting membrane; IS/OS, inner and outer segment junction of the photoreceptor cell; and RPE, retinal pigment epithelium. Scale bar, 20 μm.

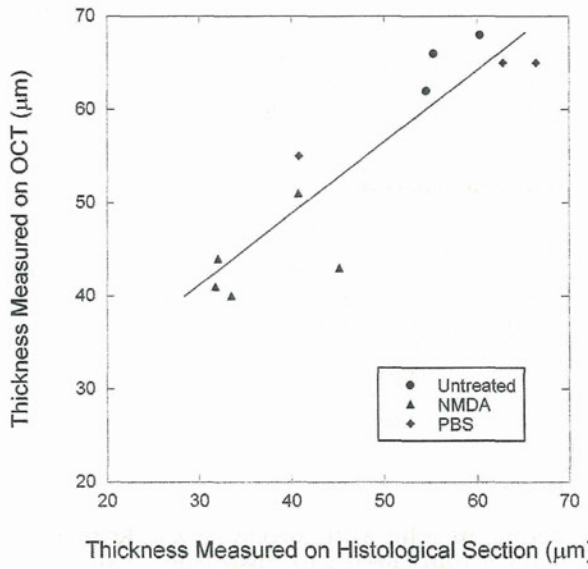

FIGURE 2. The GCC thickness measured on SD-OCT images correlated well with the thickness measured on histologic sections. OCT images (*x*-axis) versus the location-matched histologic sections (*y*-axis): $r^2 = 0.828$, $P < 0.0001$, Pearson's correlation coefficient analysis.

in the NMDA-injected eyes than in the untreated or PBS-injected eyes. However, the boundaries of the GCC (that is, the anterior boundary of the RNFL and the posterior boundary of the IPL) were relatively distinguishable, regardless of the treatment. The SD-OCT images showed that the thickness of the GCC was less in an eye injected with NMDA than in an untreated eye and an eye injected with PBS (Fig. 1A).

To determine whether GCC thickness measured on SD-OCT images correlated with the thickness measured in the histologic sections, it was measured on both the SD-OCT images and the corresponding location-matched histologic sections in the eyes injected with NMDA or PBS, and in untreated eyes. The GCC thickness measured on the SD-OCT images significantly correlated with that measured in the location-matched histologic sections ($n = 11$, $r^2 = 0.828$, $P < 0.0001$, Pearson's correlation coefficient analysis; Fig. 2). The mean GCC thickness measured on the SD-OCT images was significantly larger than that measured on the histologic retinal sections ($P = 0.027$). Thus, the images obtained with speckle noise-reduced SD-OCT were clear enough to distinguish each retinal layer and correlated highly with the histologic sections, both in healthy and damaged mouse retinas.

Correlation between GCC Thickness Measurements on Radial and Circular Scans

To evaluate GCC thickness around the optic disc, we performed six radial scans through the center of the optic nerve head and one circular scan around the optic nerve head in eyes injected with NMDA. Along each radial scan, we calculated the mean GCC thickness and averaged the values measured on all six radial scans. We also calculated GCC thickness on a circular scan image. The mean GCC thickness on the radial scans was compared with that on the circular scan during progressive RGC degeneration. We found a strong association between the GCC thickness measures on radial and circular scans ($r^2 = 0.908$, $P < 0.001$, Pearson's correlation coefficient analysis; Fig. 3). Taking a measurement on the circular scan image was simpler and faster than taking one on the radial scans; as a result, in the following experiments, we used GCC thickness measured on single circular scan images as the representative GCC thickness in mouse retinas.

Further, we calculated ICCs to assess the intradelineator and interdelineator reliability of the manual measurement of GCC thickness on the circular scans on days 0 and 14 (for each, $n = 15$). The intradelineator ICCs were 0.842 and 0.971 on day 0, and the interdelineator ICCs were 0.886 and 0.989 on day 14. All these ICC values are considered almost perfect according to the report of Landis and Koch.[29]

Imaging of CFP-Positive RGCs in Thy 1-CFP Mice by scSLO

For imaging individual RGCs, we performed scSLO of the retinas of Thy 1-CFP transgenic mice.[20] On the scSLO images, both brightly and weakly fluorescent cells of different sizes (Figs. 4A, left; 5A) were observed, a result consistent with the histologic findings of Raymond et al.[30] The CFP-positive cells were manually counted within four square areas at a distance of 830 μm from the center of the optic nerve head on the scSLO images (Fig. 5A, white squares). The distance of 830 μm was chosen as the shortest distance from the optic nerve head at which the CFP-positive cells could be accurately counted, without any influence of the retinal vessels. When an area closer to the optic nerve head is chosen, the large number of retinal vessels, which hide the CFP-positive cells from view, are included in the counting area. In addition, the density of RGCs and retinal nerve fiber bundles is higher as the area is close to the optic nerve head, which makes it difficult to precisely count the number of cells, particularly dark or small cells. The CFP-positive cells in GCL include displaced amacrines, and the displaced amacrines are small, with CFP fluorescence weaker than that of RGCs.[30] To exclude the displaced amacrines from the enumeration, we used the number of CFP-expressing cells, except for the weakly fluorescent small cells as the number of RGCs for the subsequent time-course and dose-dependence analyses of RGCs (see the Discussion section).

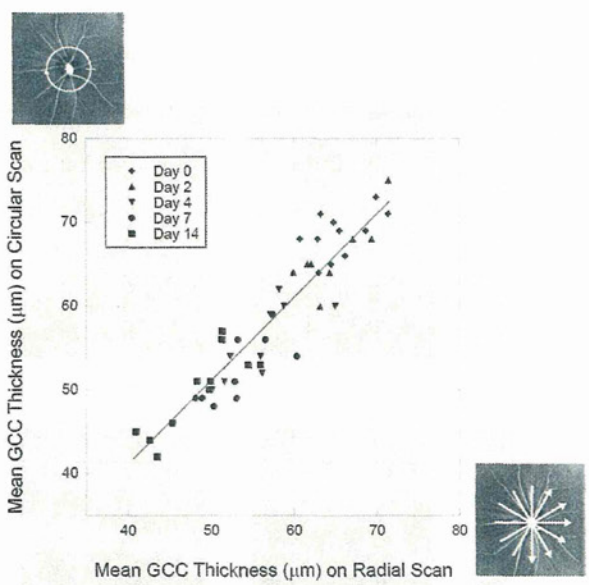

FIGURE 3. GCC thickness measured on a circular scan correlated well with the thickness measured on radial scans. GCC thickness measured on radial scans (*x*-axis) versus that on a circular scan (*y*-axis): $r^2 = 0.908$, $P < 0.001$, Pearson's correlation coefficient analysis.

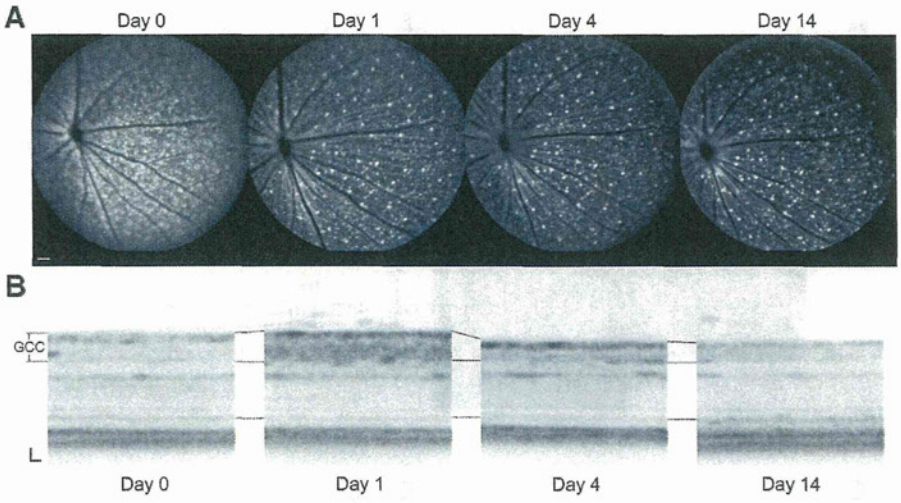

FIGURE 4. Simultaneous and longitudinal evaluation of the RGCs and the inner retinal layers after NMDA injection. (**A**) Images of Thy 1-CFP-positive RGCs using scSLO before (day 0) and after (days 1, 4, and 14) NMDA (20 nanomoles) injection. (**B**) Images acquired with speckle noise-reduced SD-OCT in the identical eye. Scale bar: (**A**) 100 μm; (**B**) 20 μm.

Time-Dependent Changes in the Number of RGCs and GCC Thickness in Identical Eyes after NMDA Injection

Next, we examined the time-dependent changes of the RGCs and the GCC thickness in the identical eyes after NMDA injection in Thy 1-CFP transgenic mice in detail. Simultaneous imaging by scSLO and SD-OCT was performed, and the number of RGCs (on scSLO) and the GCC thickness (on SD-OCT) were evaluated in the identical eyes at multiple time points. Figure 4 shows representative scSLO and SD-OCT images of a mouse eye before and after intravitreal injection of NMDA (20 nanomoles). Drastic reduction in the number of fluorescent spots was evident as early as 1 day after injection (day 1), compared with the number before injection (day 0), and then there seemed to be no change in the number of bright fluorescent spots from days 1 to 14 (Fig. 4A). Figure 5B shows the time-dependent changes in the number of CFP-expressing RGCs in mice injected with NMDA (20 nanomoles) and PBS. Although the number in the control eyes injected with PBS remained unchanged during the examination period, the mean number of RGCs in the eyes injected with NMDA dramatically decreased at day 1 (27.1% ± 7.6% [mean ± SD] of the preinjection level) and then slightly decreased from days 1 to 14 (Figs. 5B, 5D). After 14 days of NMDA injection, the number of CFP-positive RGCs decreased to 20.2% of the preinjection level. The number of RGCs in eyes injected with NMDA was significantly less than that in eyes injected with PBS after day 1 ($P < 0.0001$). To determine whether RGC loss followed a pattern at the early time points, we assessed the remaining CFP-positive RGCs in each quadrant on day 1 and found that the mean numbers were similar and did not show significant differences among the quadrants ($P = 0.886$, one-way ANOVA); the mean numbers were 19.1 ± 2.4, 17.3 ± 6.3, 17.8 ± 4.2, and 18.1 ± 5.7 (27.1%, 24.7%, 24.9%, and 26.3% of the preinjection level, respectively) in the superior, inferior, temporal, and nasal quadrants, respectively. Thus, the RGC loss on day 1 may be characterized by regional uniformity.

On the other hand, GCC thickness on the SD-OCT images did not appear to be thinned 1 day after NMDA injection and was apparently thinned from day 4 onward (Fig. 4B). In eyes injected with NMDA, the mean GCC thickness increased at day 1 ($P < 0.0001$, compared to day 0) and then started to decrease (Fig. 5C). After day 4, the GCC was significantly thinner than that before injection ($P < 0.0001$). There was a similar increase in GCC thickness in PBS control eyes at day 1 ($P = 0.01$). The GCC thickness decreased to preinjection levels at day 4 and remained unchanged thereafter through day 14 in the control eyes.

The relationship between the percentage reduction of the number of the RGCs and GCC thickness is shown in Figure 5D. One day after NMDA injection, the number of RGCs significantly decreased (to 27.1% ± 7.6%; mean ± SD). On the other hand, GCC thickness increased to 110.3% ± 6.1% on day 1. The RGCs only slightly decreased from days 1 to 14 (24.1% ± 4.5%, 22.7% ± 4.8%, 22.5% ± 4.3%, and 20.2% ± 5.1% compared to day 0, on days 2, 4, 7, and 14, respectively). In contrast, GCC thickness on day 2 was almost the same as that on day 0 (99.1% ± 6.5% of the preinjection level), then gradually decreased throughout the examination period (81.7% ± 4.3%, 75.6% ± 3.1%, and 71.4% ± 4.7% on days 4, 7, and 14, respectively). These results indicate that the decrease in the number of CFP-positive RGCs was followed by the thinning of the inner retinal layers.

Histologic Evaluation of the Effect of CFP Downregulation and Displaced Amacrines on scSLO Imaging after NMDA-Induced Injuries

There may be two problems in using Thy 1-CFP transgenic mice for monitoring RGCs: (1) the existence of displaced amacrine cells expressing CFP in GCL, as stated above and (2) CFP downregulation that occurs before RGC death. To study the response of the displaced amacrines to NMDA insult and the influence of these cells on our scSLO results, we performed immunohistochemical staining by using an anti-GFP antibody to detect CFP-positive cells and anti-HPC-1 to detect amacrines in the paraffin-embedded sections (Supplementary Fig. S1 and Supplementary Table S1, http://www.iovs.org/lookup/suppl/doi:10.1167/iovs.10-6654/-/DCSupplemental). The percentages of GFP-positive cells of all cells in the GCL were 83.0% at day 0 and 24.8% at day 14. The percentage of GFP-positive/CFP-negative (cells that possibly lost weak CFP fluorescence during sample preparation) of all GFP-positive cells was 2.6% at day 0 and 2.4% at day 14 in the frozen sections. These results suggest that GFP staining and fluorescence of CFP are almost identical and that the anti-GFP antibody is suitable for detection of CFP-positive cells (Supplementary Fig. S1A, http://www.iovs.org/lookup/suppl/doi:10.1167/iovs.10-6654/-/DCSupplemental). On day 0, the number of HPC-1-positive/GFP-positive cells in the GCL (displaced amacrines) was 20.0 ± 2.0 (6.5% of all the GFP-positive cells). After 14 days of NMDA injection, the number of HPC-1-positive/GFP-positive cells slightly decreased (15.7% ± 1.5%; 78.5% of the preinjection level, 34.6% of the remaining GFP-positive cells)

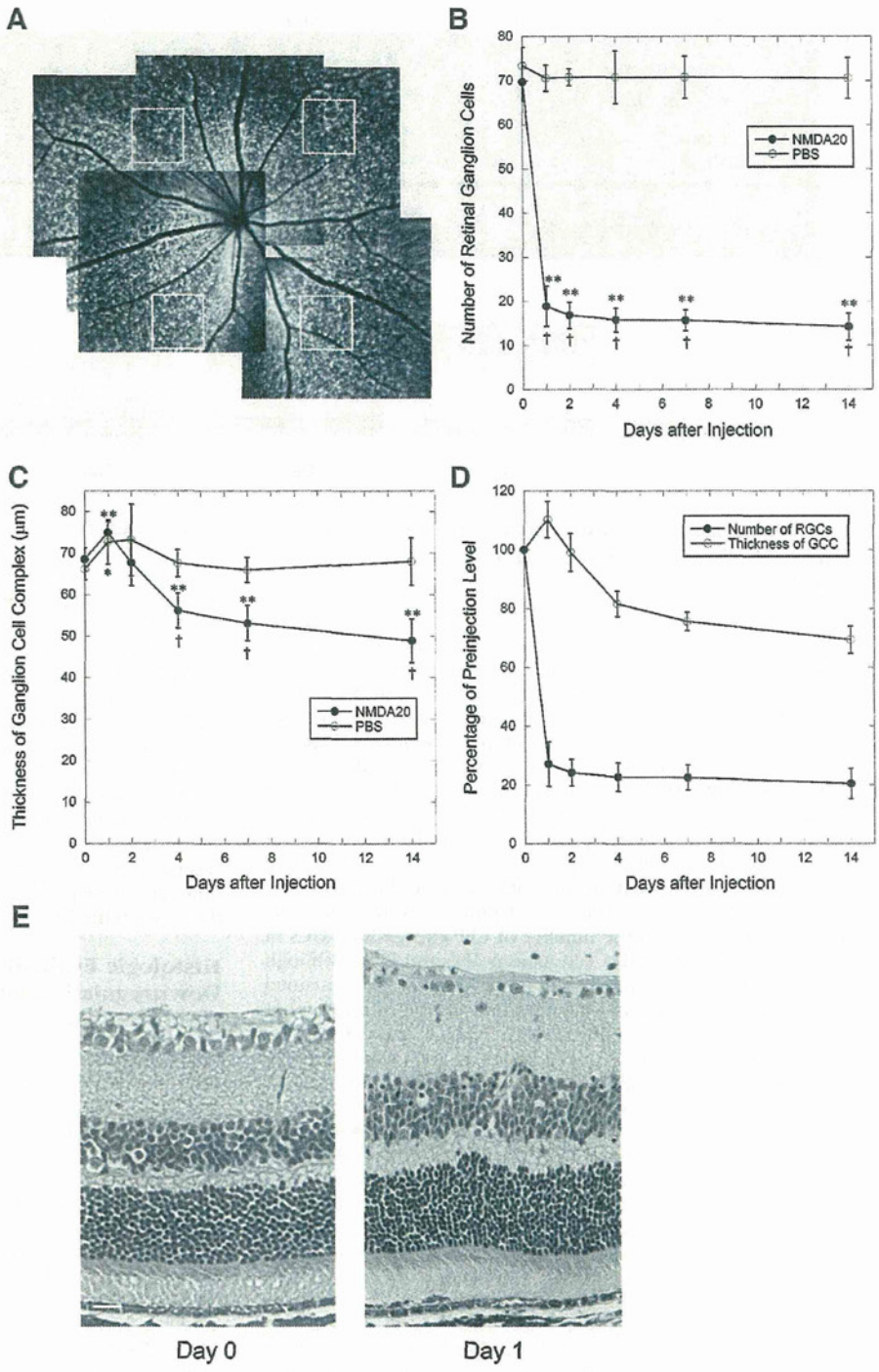

FIGURE 5. Time-dependent changes in the number of RGCs and the GCC thickness after NMDA injection. (**A**) A combined scSLO image of an untreated Thy 1-CFP mouse. The white squares (310-μm squares) indicate areas in which CFP-positive RGCs were counted. Longitudinal changes in the number of RGCs (**B**) and in GCC thickness (**C**) in mice injected with PBS and 20-nanomoles NMDA (for each, $n = 15$). (**D**) The percentage of RGCs and GCC thickness in the postoperative period versus that in the preoperative period. Error bars indicate SD. $^{*}P < 0.05$; $^{**}P < 0.0001$ compared with the preinjection level (paired t-test). †$P < 0.0001$ compared between eyes injected with NMDA and PBS (t-test). (**E**) Images obtained on days 0 and 1 of retinal sections from eyes injected with NMDA (20 nanomoles) and stained with HE. The retina on day 1 appears to be thickened and particularly the IPL appears swollen. RGCs appear to be fewer on day 1, compared with day 0. Scale bar, 20 μm.

(Supplementary Fig. S1B, http://www.iovs.org/lookup/suppl/doi:10.1167/iovs.10-6654/-/DCSupplemental). Next, we focused on HPC-1-negative cells in the GCL, which could be considered to be mainly RGCs, to reveal the effect of CFP downregulation on the scSLO results. On day 1 after NMDA injection, HPC-1-negative cells decreased to 65.2% of the preinjection level. HPC-1-negative/GFP-positive cells decreased to 34.6% of the preinjection level. In contrast, HPC-1-negative/GFP-negative cells increased to 258.3% of the preinjection level. To confirm that the HPC-1-negative/GFP-negative cells contain RGCs, we performed triple immunostaining for HPC-1, Brn3 (an antibody for retinal ganglion cells[28]), and GFP (Supplementary Fig. 1C, http://www.iovs.org/lookup/suppl/doi:10.1167/iovs.10-6654/-/DCSupplemental). There were Brn3-positive cells that stained negative for HPC-1 and GFP cells, both before and after NMDA injection, suggesting that retinal ganglion cells are included in the HPC-1-negative/GFP-negative cell population. These results suggested that although CFP downregulation occurred in some cells, the number of RGCs indeed decreased as early as 1 day after NMDA injection. To further confirm that

RGC loss preceded reduction in GCC thickness, we compared the hematoxylin-eosin (HE)-stained retinal sections between days 0 and 1 (Fig. 5E). On day 1, the retina, particularly the IPL, appeared to be thickened. On the other hand, on day 1, the cells in the GCL decreased to 72.6% of that on day 0, as counted on the histologic sections. From these histologic observations, we confirmed that rapid loss of RGCs preceded the thinning of the inner retinal layers.

Dose- and Time-Dependent Changes in the Number of RGCs and GCC Thickness in Identical Eyes after NMDA Injection

To clarify the difference in the severity and time course of the damage caused by different dosage of NMDA, 1 to 20 nanomoles of NMDA (or PBS as a negative control) was injected in the eyes of Thy 1-CFP mice and examined with scSLO and SD-OCT. In eyes injected with 2 to 20 nanomoles of NMDA, the number of RGCs significantly decreased on day 1 and thereafter, whereas in the eyes injected with 1 nanomole of NMDA, RGCs only marginally decreased during the period, compared with eyes injected with PBS (Fig. 6A). Eyes injected with 10 or 20 nanomoles NMDA showed similar reductions in the number of RGCs on day 14 (28.3% and 20.2% of the preinjection level, respectively). However, the reduction was slower in eyes injected with 10 nanomoles of NMDA compared with those with 20 nanomoles of NMDA; the number of RGCs in eyes injected with 10 nanomoles of NMDA was larger than the number of RGCs in eyes injected with 20 nanomoles of NMDA on day 1 (49.5% and 27.1% of the preinjection level, respectively, $P = 0.002$ [Scheffé's test]), but was not significant on days 4 to 14. The eyes injected with 2 or 5 nanomoles of NMDA tended to show a smaller reduction in numbers compared with those injected with 10 or 20 nanomoles of NMDA throughout the postinjection period; the number of RGCs was 65.3% ($P = 0.003$) and 71.7% ($P = 0.004$) of the preinjection level, respectively, on day 1 and further decreased to 44.1% ($P < 0.0001$) and 53.7% ($P < 0.0001$) of the preinjection level, respectively, on day 14. Thus, NMDA dose dependently reduced the number of RGCs; a higher dose of NMDA induced more rapid and stronger loss of RGCs.

Consistent with the number of RGCs, 2- to 20-nanomole NMDA injections caused significant decreases in GCC thickness at day 4 and thereafter (Fig. 6B). As was the case with 20 nanomoles of NMDA injection (above), the GCC thickness did not significantly decrease until 4 days after the injection. PBS or a 1-nanomole NMDA injection did not decrease GCC thickness (Fig. 6B). In eyes injected with 5, 10, and 20 nanomoles of NMDA, GCC thickness decreased to 75.7%, 76.5%, and 71.4%, respectively, of the preinjection level on day 14; there were no statistically significant differences between the three groups (Scheffé's test). GCC thickness in eyes injected with 2 nanomoles of NMDA showed a lesser reduction (84.6% of the preinjection level) than those injected with 5 to 20 nanomoles ($P = 0.041$ vs. 5 nanomoles; $P = 0.021$ vs. 20 nanomoles) on day 14. These results show that decreases in the number of RGCs and in GCC thickness are NMDA dose dependent and that 2 nanomoles or more of NMDA is needed to induce a significant loss of RGCs and in GCC thickness.

Discussion

In this study, we used a novel, noninvasive imaging system combining scSLO and speckle noise–reduced SD-OCT to characterize the longitudinal and dose-dependent RGC degeneration induced by NMDA. Two nanomoles or more of NMDA induced rapid loss of CFP-expressing RGCs. The inner retinal layer became thin after the CFP-expressing RGCs disappeared. The NMDA-induced degeneration of RGCs and the inner retinal layers was dose-dependent.

The development of imaging instruments for clinical use provides a unique opportunity to apply these instruments to experimental animals for noninvasive, longitudinal assessment of progressive RGC damage. Recent studies have demonstrated that imaging of CFP-expressing RGCs in Thy 1-CFP transgenic mice using a blue-light confocal SLO or a fundus camera is useful for the longitudinal assessment of injuries to the bodies of RGCs in optic nerve crush and ischemia–reperfusion models.[7–9] Another study has shown that measuring RNFL thickness is also useful for longitudinally assessing axonal injuries of RGCs in an optic nerve crush model.[10] However, no studies have reported longitudinal assessments of RGC damage, both in the number of RGCs and in the thickness of the inner retinal layer by any method.

NMDA-induced excitotoxicity is a well-known model of induced RGC injury[25] and has been implicated in the pathogenesis of glaucoma. At first, we injected 20 nanomoles of NMDA into the vitreous of Thy 1-CFP mice and observed that the number of CFP-expressing RGCs decreased to less than 30% of the preinjection level as early as 1 day after injection and continued to decrease slightly from days 1 to 14 (Fig. 5). In contrast, GCC thickness increased at day 1 and then gradually decreased from days 2 to 14. This study clearly demonstrated that two distinct structural parameters (number of CFP-positive RGCs and GCC thickness), whose losses were recently established to represent RGC damage in vivo, behaved in a totally different manner during the time course of NMDA-induced RGC injury in a mouse model.

In rats, Nagata et al.[10] were not able to find RNFL thinning, even 1 week after optic nerve crush versus the 50% RGC loss that was reported in another study.[4] Although no study has directly compared the number of RGCs (based on Thy 1-CFP expression

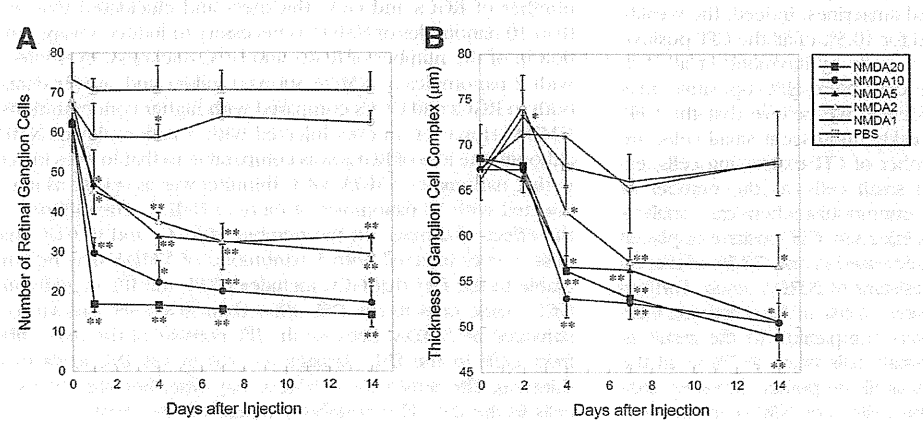

FIGURE 6. Dose- and time-dependent changes in the number of RGCs and in GCC thickness in identical eyes after NMDA injection. Longitudinal changes in the number of RGCs (A) and in GCC thickness (B) in mice injected with PBS ($n = 15$) and NMDA (1, 2, 5, 10, and 20 nanomoles; $n = 6$, $n = 10$, $n = 10$, $n = 15$, and $n = 15$, respectively). $^{*}P < 0.05$; $^{**}P < 0.0001$ compared to the preinjection level (paired t-test).

or retrograde labeling) with retinal thickness (e.g., RNFL or GCC thicknesses) in the same eyes, the studies[4,10] suggest that retinal thinning is likely the event that results from optic nerve crush-induced RGC injury. Consistently, the reduction of RGCs seen as Thy 1-CFP expression in our study, apparently occurred several days before the thinning of the inner retinal layers, particularly RNFL; however, there are several concerns regarding the interpretation of the results.

One concern regarding the temporally different patterns of reduction in the number of CFP-positive RGCs and GCC thickness is the initial inflammatory response, which can mask the thinning of the nerve fiber layers. The swelling of IPL seen in the histologic sections on day 1 suggested the existence of an inflammatory response, which may increase GCC thickness. Mild GCC thickening was also seen from 1 to 4 days after injection in the PBS-injected control eyes (Fig. 5). Therefore, the thickening may be caused by the inflammatory reaction induced by the intravitreal injection itself rather than by the NMDA injection.

Another concern regarding the temporally different patterns of reduction in the above-mentioned two parameters is the possibility of CFP downregulation that occurs before RGC death. Schlamp et al.[31] demonstrated that by 6 hours after NMDA injection, the *Thy1* mRNA levels in the RGC starts to decrease, whereas there is no apparent change in the number of the cells present in the GCL. By 48 hours, the expression level of *Thy1* mRNA or Thy1-expressing cells decreases to less than 20% of the control fellow eyes, whereas more than half of the cells remained in the GCL. Similar earlier loss of Thy 1 expression in RGCs preceding the loss of RGC numbers on histologic or imaging studies has been documented in an optic nerve crush model.[7] The early loss of Thy 1 expression is consistent with the report that the damaged RGCs undergo a shutdown of many normally expressed genes as an early step in apoptosis.[32] In our immunohistochemical analysis, 1 day after NMDA injection, GFP-positive RGCs decreased to 34.6% of the preinjection level, which was comparable to 27.1% observed on the scSLO images. On the other hand, GFP-negative RGCs increased to more than two times the preinjection level, suggesting that CFP downregulation actually occurred in some cells. However, RGCs (all the HPC-1-negative cells in GCL) indeed decreased to 65.2% of the preinjection level. Moreover, the cells in GCL, counted on the HE-stained sections on day 1, were 72.6% of the preinjection level. Therefore, although downregulation of CFP expression occurred before the disappearance of the somas of some RGCs, these observations indicate that thinning of the inner retinal layers is an event resulting from the loss of RGCs in NMDA-induced retinal injuries.

CFP expression in Thy 1-CFP mouse line has been reported to localize not only to RGCs but also to a subpopulation of displaced amacrine cells.[30] It has been reported that the displaced amacrines are small and emit weakly fluorescent signals. Therefore, we believe that weakly fluorescent small cells in the scSLO images in this study are mainly displaced amacrines. Indeed, the weakly fluorescent small cells accounted for 10.5% of all the CFP-positive cells, a finding consistent with a study by Raymond et al.,[30] in which 9.6% of the CFP-positive cells were HPC-1-positive amacrines. On the basis of this evidence, we believe that the CFP-positive cells, other than the weakly fluorescent small cells, are mainly RGCs, and used the number of CFP-expressing cells, excluding the weakly fluorescent small cells, as the number of CFP-expressing RGCs. Our immunohistochemical analysis showed that 14 days after NMDA injection, GFP-positive displaced amacrine cells (HPC-1-positive) decreased to only 78.5% of that on day 0, indicating that they are resistant to NMDA insult. Furthermore, the HPC-1-positive cells were 34.6% of the remaining GFP-positive cells on day 14; this was comparable to the result of scSLO that weakly fluorescent small cells were 46.7% of all the CFP-positive cells. Consideration of all the points, however, indicates that many of the remaining cells after NMDA insult were surviving RGCs. Thus, the RGCs that were resistant to one-time NMDA injection might account for the plateau that was seen in the time course of changes in the number of CFP-positive cells on the scSLO images in this study, although the appearance of the plateau may be partly explained by the existence of the less vulnerable displaced amacrine cells.

We also evaluated the potential difference in the vulnerability to NMDA insult among the different sizes of the RGCs using the scSLO images. Fourteen days after NMDA injection, the number of CFP-expressing large RGCs decreased to 18.8% of the preinjection level, whereas the number of CFP-expressing small RGCs decreased to 23.3% of the preinjection level. Therefore, on the basis of the size of the RGCs using scSLO images, the vulnerability to NMDA did not significantly differ between the cell types.

In clinical studies, circumpapillary retinal nerve fiber layer (cpRNFL) thickness is widely used to discriminate eyes with glaucoma. In human and mouse eyes, assessment of the RNFL thickness on a circular scan around the optic nerve head appears ideal for evaluating RGC damage because it is capable of detecting all RGC axons that converge toward the optic nerve head in both species. However, RNFLs in mice are much thinner than those of humans and are much more difficult to measure, particularly in damaged retinas. In this study, besides GCC thinning in the damaged retinas, the layer boundaries also became unclear, probably because the loss of the somas, axons, and dendrites of RGCs and changes in glial components decreased the reflectivity of the diminished RNFL, GCL, and IPL. The GCC is an alternative to the RNFL for assessing RGC damage, since the GCC includes RGC axons as RNFL and RGC somas as GCL. GCC is thicker than RNFL only, allowing easier delineation in all eyes. In patients with glaucoma, GCC thickness in the macula has been shown to have glaucoma discriminating ability that is comparable to cpRNFL thickness.[15–18] However, mouse eyes do not have a macula. Therefore, instead of measuring macular GCC thickness or cpRNFL thickness, we thought it practically appropriate to use GCC thickness around the optic nerve head to detect glaucomatous damage. Because it is uncertain which scan pattern for sampling is appropriate for GCC measurements in mice, we compared the most standard scan patterns around the optic nerve head; the circular scan versus radial scans. We found a strong correlation between these scan patterns. In addition, we were able to detect a characteristic slow decrease in GCC thickness on a circular scan in the mouse eyes injected with NMDA consistent with the results of previous studies.[10] We also confirmed the reliability of the manual measurement of GCC thickness. These observations show that GCC thickness on a circular scan around the optic disc is an ideal and useful parameter for evaluating RGC damage in mice.

Then, we examined NMDA dose-dependent changes in the number of RGCs and GCC thickness and elucidated that more than 10 nanomoles of NMDA is necessary to induce severe reduction in of the number of RGCs and GCC thickness. Eyes injected with 2 nanomoles of NMDA showed milder and slower damage both to RGCs and GCCs compared with higher concentrations of NMDA. However, in eyes injected with 5 nanomoles of NMDA, although the loss of RGCs was comparable to that in eyes injected with 2 nanomoles NMDA, GCC thinning was as severe as in eyes injected with 10 nanomoles or more of NMDA. The difference in the effect of damage on the number of RGCs and in GCC thickness in eyes injected with 5 nanomoles of NMDA may be attributable to the fact that GCC includes RNFL and IPL in addition to GCL. Some cells in the INL other than RGCs are known to be damaged by NMDA. Because the IPL consists of the nerve fibers from cells in the INL, damage to cells in the INL leads to IPL thinning. The sensitivity to NMDA may differ between RGCs and cells in the INL. This possibility remains to be clarified.

Application of retinal imaging technologies to mice, particularly those with genetic cellular markers, allows noninvasive longitudinal assessment of neuronal damage such as loss of cell bodies and tissue atrophy. Experimental mouse models are most widely used to investigate the pathophysiology of human diseases; various transgenic and knockout mice as well as natural mutants are available for use in the investigation of the role of a molecule in vivo. The noninvasive nature of this approach does not require animals to be euthanized and enables us to examine exactly the same region in the same eye via in vivo sequential imaging, allowing for use of a minimal number of animals. Compared with histologic methods, our double-imaging approach in particular has a great advantage in monitoring both the individual RGC loss and the RGC-related layer thinning on sectional images in the same diseased eyes. Our findings with regard to the different time courses of the two RGC-related parameters were strengthened by measuring both parameters simultaneously in the identical eyes. Thus, the simultaneous imaging of two parameters in the mouse fundus, as shown in this study, would potentially be widely used as a useful tool for basic and translational research of the examination of pathologic mechanisms of RGC damage, as well as for investigation of new treatments for glaucoma.

In summary, we were able to show time-dependent changes in Thy 1-CFP-expressing RGCs and GCC thickness in the identical eyes with an NMDA-induced RGC injury by using a combined system of scSLO and speckle noise–reduced SD-OCT. We found that the reduction in these two parameters show different time courses. Co-monitoring of CFP-expressing RGCs and GCC thickness in mice would contribute to investigation of the longitudinal profile of RGC degeneration.

Acknowledgments

The authors thank Yuri Terado, Noriko Suzuki, Michiko Tsuji, and Keiko Kuroiwa for their technical assistance, Akiko Hirata for her contribution to the reliability assessment of the manual measurement of GCC thickness on SD-OCT images, and Gerhard Zinser for useful discussions of the Multiline instrument.

References

1. Quigley HA. Number of people with glaucoma worldwide. *Br J Ophthalmol.* 1996;80:389–393.
2. Fechtner RD, Weinreb RN. Mechanisms of optic nerve damage in primary open angle glaucoma. *Surv Ophthalmol.* 1994;39:23–42.
3. Cordeiro MF, Guo L, Luong V, et al. Real-time imaging of single nerve cell apoptosis in retinal neurodegeneration. *Proc Natl Acad Sci U S A.* 2004;101:13352–13356.
4. Higashide T, Kawaguchi I, Ohkubo S, Takeda H, Sugiyama K. In vivo imaging and counting of rat retinal ganglion cells using a scanning laser ophthalmoscope. *Invest Ophthalmol Vis Sci.* 2006; 47:2943–2950.
5. Srinivasan VJ, Ko TH, Wojtkowski M, et al. Noninvasive volumetric imaging and morphometry of the rodent retina with high-speed, ultrahigh-resolution optical coherence tomography. *Invest Ophthalmol Vis Sci.* 2006;47:5522–5528.
6. Leung CK, Lindsey JD, Crowston JG, et al. In vivo imaging of murine retinal ganglion cells. *J Neurosci Methods.* 2008;168:475–478.
7. Leung CK, Lindsey JD, Crowston JG, Lijia C, Chiang S, Weinreb RN. Longitudinal profile of retinal ganglion cell damage after optic nerve crush with blue-light confocal scanning laser ophthalmoscopy. *Invest Ophthalmol Vis Sci.* 2008;49:4898–4902.
8. Murata H, Aihara M, Chen YN, Ota T, Numaga J, Araie M. Imaging mouse retinal ganglion cells and their loss in vivo by a fundus camera in the normal and ischemia-reperfusion model. *Invest Ophthalmol Vis Sci.* 2008;49:5546–5552.
9. Leung CK, Lindsey JD, Chen L, Liu Q, Weinreb RN. Longitudinal profile of retinal ganglion cell damage assessed with blue-light confocal scanning laser ophthalmoscopy after ischaemic reperfusion injury. *Br J Ophthalmol.* 2009;93:964–968.
10. Nagata A, Higashide T, Ohkubo S, Takeda H, Sugiyama K. In vivo quantitative evaluation of the rat retinal nerve fiber layer with optical coherence tomography. *Invest Ophthalmol Vis Sci.* 2009; 50:2809–2815.
11. Fischer MD, Huber G, Beck SC, et al. Noninvasive, in vivo assessment of mouse retinal structure using optical coherence tomography. *PLoS One.* 2009;4:e7507.
12. Guo L, Normando EM, Nizari S, Lara D, Cordeiro MF. Tracking longitudinal retinal changes in experimental ocular hypertension using the cSLO and spectral domain-OCT. *Invest Ophthalmol Vis Sci.* 2010;51:6504–6513.
13. Schmitt JM, Xiang SH, Yung KM. Speckle in optical coherence tomography. *J Biomed Opt.* 1999;4:95–105.
14. Hangai M, Yamamoto M, Sakamoto A, Yoshimura N. Ultrahigh-resolution versus speckle noise-reduction in spectral-domain optical coherence tomography. *Opt Express.* 2009;17:4221–4235.
15. Ishikawa H, Stein DM, Wollstein G, Beaton S, Fujimoto JG, Schuman JS. Macular segmentation with optical coherence tomography. *Invest Ophthalmol Vis Sci.* 2005;46:2012–2017.
16. Tan O, Li G, Lu AT, Varma R, Huang D. Advanced imaging for glaucoma study group: mapping of macular substructures with optical coherence tomography for glaucoma diagnosis. *Ophthalmology.* 2008;115:949–956.
17. Tan O, Chopra V, Lu AT, et al. Detection of macular ganglion cell loss in glaucoma by Fourier-domain optical coherence tomography. *Ophthalmology.* 2009;116:2305–2314.
18. Seong M, Sung KR, Choi EH, et al. Macular and peripapillary retinal nerve fiber layer measurements by spectral domain optical coherence tomography in normal-tension glaucoma. *Invest Ophthalmol Vis Sci.* 2010;51:1446–1452.
19. Shaner NC, Steinbach PA, Tsien RY. A guide to choosing fluorescent proteins. *Nat Methods.* 2005;2:905–909.
20. Feng G, Mellor RH, Bernstein M, et al. Imaging neuronal subsets in transgenic mice expressing multiple spectral variants of GFP. *Neuron.* 2000;28:41–51.
21. Morris R. Thy-1 in developing nervous tissue. *Dev Neurosci.* 1985; 7:133–160.
22. Barnstable CJ, Drager UC. Thy-1 antigen: a ganglion cell specific marker in rodent retina. *Neuroscience.* 1984;11:847–855.
23. Siliprandi R, Canella R, Carmignoto G, et al. N-methyl-D-aspartate-induced neurotoxicity in the adult rat retina. *Vis Neurosci.* 1992; 8:567–573.
24. Vorwerk CK, Lipton SA, Zurakowski D, Hyman BT, Sabel BA, Dreyer EB. Chronic low-dose glutamate is toxic to retinal ganglion cells: toxicity blocked by memantine. *Invest Ophthalmol Vis Sci.* 1996;37:1618–1624.
25. Nickells RW. Retinal ganglion cell death in glaucoma: the how, the why, and the maybe. *J Glaucoma.* 1996;5:345–356.
26. Li Y, Schlamp CL, Nickells RW. Experimental induction of retinal ganglion cell death in adult mice. *Invest Ophthalmol Vis Sci.* 1999;40:1004–1008.
27. Ooto S, Hangai M, Sakamoto A, et al. Three-dimensional profile of macular retinal thickness in normal Japanese eyes. *Invest Ophthalmol Vis Sci.* 2010;51:465–473.
28. Soto I, Brian E, Buckingham P, et al. Retinal ganglion cells downregulate gene expression and lose their axons within the optic nerve head in a mouse glaucoma model. *J Neurosci.* 2008;28:548–561.
29. Landis JR, Koch GG. The measurement of observer agreement for categorical data. *Biometrics.* 1977;33:159–174.
30. Raymond ID, Vila A, Huynh UC, Brecha NC. Cyan fluorescent protein expression in ganglion and amacrine cells in a thy1-CFP transgenic mouse retina. *Mol Vis.* 2008;14:1559–1574.
31. Schlamp CL, Johnson EC, Li Y, Morrison JC, Nickells RW. Changes in Thy1 gene expression associated with damaged retinal ganglion cells. *Mol Vis.* 2001;7:192–201.
32. Miller TM, Moulder KL, Knudson CM, et al. Bax deletion further orders the cell death pathway in cerebellar granule cells and suggests a caspase-independent pathway to cell death. *J Cell Biol.* 1997;139:205–217.

Gene Expression Patterns 12 (2012) 36–45

Contents lists available at SciVerse ScienceDirect

Gene Expression Patterns

journal homepage: www.elsevier.com/locate/gep

Spatio-temporal expression pattern of the NatB complex, Nat5/Mdm20 in the developing mouse brain: Implications for co-operative *versus* non-co-operative actions of Mdm20 and Nat5

Kyoji Ohyama [a,*], Kunihiko Yasuda [a], Kazuko Onga [a], Akira Kakizuka [b], Nozomu Mori [a,*]

[a] *Department of Anatomy and Neurobiology, Graduate School of Biomedical Sciences, Nagasaki University, 1-12-4 Sakamoto, Nagasaki 852-8523, Japan*
[b] *Laboratory of Functional Biology, Kyoto University Graduate School of Biostudies, Kyoto 606-8501, Japan*

ARTICLE INFO

Article history:
Received 2 June 2011
Received in revised form 1 November 2011
Accepted 2 November 2011
Available online 10 November 2011

Keywords:
Nat
Mdm20
Acetylation
Post-translation
Mouse
Brain
Neuron

ABSTRACT

The NatB complex, Nat5/Mdm20 acetyltransferase mediates *N*-acetylation to control cell cycle progression and actin dynamics in yeast. As yet, little is known about the expression pattern of Mdm20 and Nat5 in multi-cellular organisms. Here we show that Mdm20 is highly expressed in mouse embryonic brain. At E11.5, Mdm20 was widely expressed in both neural progenitors and early differentiating neurons, whereas Nat5 was expressed in Sox1/3+/Mdm20+ neural progenitors. By E14.5, both Mdm20 and Nat5 were downregulated in most ventricular zone neural progenitors, whereas both proteins were found in differentiating neurons and co-expression was maintained at E18.5 in derivatives of these cells, such as midbrain dopaminergic (DA) neurons and septal neurons. These data suggest that Nat5/Mdm20 complex-mediated acetylation may play a role in the proliferation and differentiation of neural progenitors. Intriguingly, our data also showed that Mdm20 is not always co-expressed with Nat5 in all differentiated neurons, for example deep cerebellar neurons. Moreover, detailed examination of the subcellular localization of Mdm20 and Nat5 in cultured Nat5+/Mdm20+ midbrain DA neurons revealed that Mdm20 is also not necessarily co-localized with Nat5 within neurons. Given that Nat5 is only a known member of Nat family protein that interacts with Mdm20, our data imply that Mdm20 may function either with an unidentified Nat protein partner(s) or possibly in a Nat-independent manner.

Post-translational modification of proteins is critically important in biology and expands both the structural and functional diversity of proteins, contributing to both evolutionary divergence and population diversity (Magalon et al., 2008; Arnesen et al., 2009). Two particular protein modifications, acetylation and phosphorylation, play key roles in a wide range of biological events, including tissue development (Kouzarides, 2000; Choudhary et al., 2009; Sadoul et al., 2010). The sculpting of tissue morphology over time is also dependent on the spatial and temporal control of gene transcription (Dessaud et al., 2007; Ohyama et al., 2008; Pearson et al., 2011), and indeed acetylation and phosphorylation often co-operate to modulate protein activities, which in turn modulate gene transcription (Sims and Reinberg, 2008; Lau and Cheung, 2011). For instance, a lysine acetyltransferase (KAT) – formerly called HAT (histone acetyltransferase) – mediates acetylation of the internal lysine residues of histones which, coupled with histone phosphorylation and methylation, controls the de-repression of polycomb-silenced genes, whose temporally-regulated functions are crucial to development (Lau and Cheung, 2011). Conversely, nuclear-located histone deacetylases (HDACs) mediate the repression of gene transcription by the polycomb complex (Sadoul et al., 2010; Garrick et al., 2008).

Recent studies extended the view that reversible acetyl modification of proteins at internal lysine residues is not limited to events in the nucleus but also occurs in the cytoplasm, controlling important biological processes such as translation, cellular apoptosis, motility, and protein quality control (Creppe et al., 2009; Ctalano et al., 2007; Kim et al., 2006; Sadoul et al., 2010). For instance, αTAT1 is responsible for the acetylation of α-tubulin, whereas HDAC6 functions as a α-tubulin deacetylase exclusively in the cytoplasm (Shida et al., 2010; Hubbert et al., 2002). As a consequence, these modifications regulate microtubule stability, and thus cell motility, independent of both histone metabolism and gene transcription (Hubbert et al., 2002). While to date several hundreds of cytosolic proteins have been found to undergo an acetyl modification, the biological significance of this remains to be elucidated (Kim et al., 2006; Choudhary et al., 2009).

N-terminal acetylation is another enzyme-catalyzed reaction whereby N-terminal residues accept the acetyl group from acetyl-CoA. While it takes a place on approximately 80–90% of

* Corresponding authors. Tel./fax: +81 95 819 7017.
E-mail addresses: kyohyama@nagasaki-u.ac.jp (K. Ohyama), morinosm@nagasaki-u.ac.jp (N. Mori).

1567-133X/$ - see front matter © 2011 Elsevier B.V. All rights reserved.
doi:10.1016/j.gep.2011.11.001

cytosolic proteins in mammals, less attention has been paid to its function (Ametzazurra et al., 2008; Polevoda and Sherman, 2003; Polevoda et al., 2008, 2009). Emerging evidence suggests that an N-terminal acetylation of nascent polypeptides synthesized on polyribosomes plays a pivotal role in cellular homeostasis (Starheim et al., 2008; Arnesen et al., 2010). Based on *in vitro* studies, this modification has been proposed to influence protein function, stability, and subsequent modifications that include phosphorylation. It has been shown to control cell proliferation and protein quality to prevent the aggregation of abnormal proteins (Starheim et al., 2008; Arnesen et al., 2010). Biochemical studies have also shown that in the nervous system serotonin undergoes N-terminal acetyl modification and subsequent conversion to melatonin, thereby regulating the synthesis and metabolism of serotonin as a feedback system (Issac et al., 1990; Miguez et al., 1997; Sugiura et al., 2003). Nonetheless, due to the shortage of *in vivo* studies, it is still not well understood how N-terminal acetylation controls biological events in tissues.

N-acetyltransferase (Nat) complexes are composed of catalytic and auxiliary subunits, and are responsible for the enzymatic reaction to acetylate cytosolic proteins (Ametzazurra et al., 2008; Polevoda and Sherman, 2003; Polevoda et al., 2008, 2009). In yeast, five *N*-alpha-acetyltransferases (NATs), i.e. NatA-E, have been described as catalytic subunits, depending on the distinct amino acid sequences at N-termini they recognize. NatA, NatB, and NatC are three major *N*-acetyltransferases, whereas the substrates for NatD and E are poorly identified. As auxiliary subunits of three major Nat complexes (i.e. NatA, NatB, and NatC), Nat1p, Mdm20p, Mak31p have been identified, respectively in yeast.

In mammals, the NatA complex is composed of a catalytic subunit, ARD1 (arrested defective 1) and an auxiliary subunit NATH (*N*-acetyltransferase human). In the developing mouse brain, both ARD1 and NATH are highly expressed in proliferating progenitors and their expression is downregulated as they differentiate (Gendron et al., 2000; Sugiura et al., 2003). A recent study also showed that NatA complex ARD1-NAT1 is required for the dendritic arbolization of Purkinje cells in the postnatal cerebellum (Ohkawa et al., 2008). These studies clearly indicate that N-terminal acetyl-modification of proteins plays an important role in both the developing and mature brain.

Mdm20 (a regulator of mitochondrial distribution and morphology) is an auxiliary subunit of the NatB complex, the second major acetyltransferase and binds catalytic subunit Nat3 in yeast (Starheim et al., 2008; Ametzazurra et al., 2008; Polevoda and Sherman, 2003; Polevoda et al., 2009). The yeast NatB complex, Mdm20/Nat3 regulates tropomyosin-actin interactions (Singer and Shaw, 2003). In human cells, the NatB acetyltransferase complex is composed of Mdm20 and Nat5 (the human orthologue of yeast Nat3) and has been shown to be essential for cell cycle progression. (Starheim et al., 2008). Given that mouse Nat5 is the closest Nat family protein to human Nat5 and yeast Nat3, mMdm20 and mNat5 are likely to be the auxiliary and catalytic subunits of a mouse NatB acetyltransferase complex, respectively (Starheim et al., 2008; Ametzazurra et al., 2008; Polevoda and Sherman, 2003; Polevoda et al., 2008).

Although *in vitro* studies have suggested the importance of NatB complexes in fundamental cellular events, namely cell proliferation and cytoskeletal organization, none of the subunit proteins

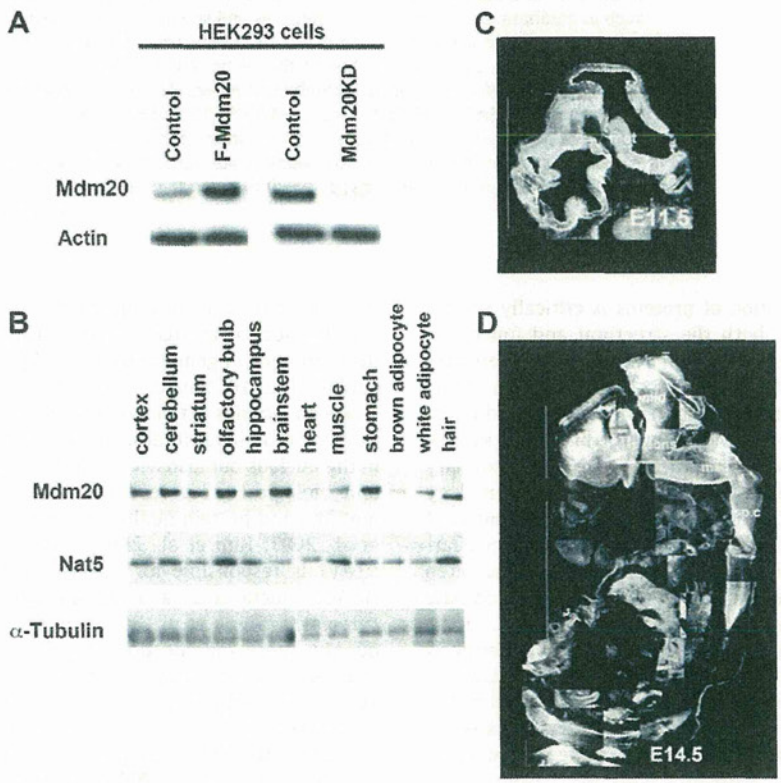

Fig. 1. Mdm20 is highly expressed in the embryonic and adult mouse brains. (A) Western blot of human embryonic kidney (HEK) 293 cells lysates using anti-Mdm20 rabbit polyclonal antibody. When a flag-tagged human Mdm20 was overexpressed (F-Mdm20), an increased expression of Mdm20 was detected. Conversely, an endogenous expression of human Mdm20 was decreased when human Mdm20 was knocked down by human Mdm20 siRNA (Mdm20KD). Western blot of β-actin was used as an internal control. (B) Western blot analysis of adult mouse tissues. Both Mdm20 and Nat5 are highly expressed in the brain (cerebral cortex, cerebellum, striatum, olfactory bulb, hippocampus, brainstem), stomach, and hair, compared to their expression level in heart and muscle. α-Tubulin expression was monitored as internal controls. (C and D) Immunofluorescent labeling of Mdm20 in mouse embryo at E11.5 (C) and E14.5 (D). Sagittal section of the mouse embryonic brain shows that Mdm20 is highly expressed in the brain and spinal cord. tel; telencephalon, mes; mesencephalon, dien; diencephalon, bs; brainstem, str; striatum, sp.c; spinal cord.

have been investigated for their function *in vivo*. In fact, the expression patterns of Mdm20 and Nat5 have not been examined systematically in multi-cellular organisms. Here we document for the first time the distribution pattern of Mdm20 protein in the developing mouse brain and compare it with that of Nat5. We further describe their subcellular localization and discuss their possible functions in the developing brain.

1. Results

1.1. Mdm20 is highly expressed both in the developing and adult mouse brain

We first generated a rabbit polyclonal antibody against a carboxy-terminal sequence of the Mdm20 protein conserved between human and mouse. Using human embryonic kidney (HEK) 293 cell lysates, we performed Western blot analysis of Mdm20 and detected a specific single band, which corresponds to the predicted molecular weight 120 kD (Fig. 1 and data not shown). The anti-Mdm20 antibody also detected either the increase or decrease of Mdm20 expression when Flag-tagged full length of Mdm20 cDNA (F-Mdm20) was overexpressed or Mdm20 was knocked down by siRNA for Mdm20 (Mdm20KD), respectively (Fig. 1A). These data confirmed the specificity of the anti-Mdm20 antibody.

We next examined the tissue distribution of Mdm20 protein in adult mice. Western blot analysis demonstrated that both Mdm20 and Nat5 were highly expressed in the brain, stomach, and hair (Fig. 1B). Similar to its prominent expression in the adult brain, Mdm20 was found to be highly expressed in the embryonic brain as evidenced by immunofluorescent staining (Fig. 1C and D). Mdm20 expression was also evident in dorsal root ganglia, muscles, chondrocytes, skin, and heart (data not shown).

1.2. Mdm20 and Nat5 expression in neural progenitors and differentiating neurons of mouse embryonic brain

As Mdm20 is a component of the NatB complex, we further investigated the expression pattern of Mdm20 and compared it with that of Nat5 in the developing mouse brain. At E11.5 Mdm20 was widely expressed, including in most proliferating cell nuclear antigen (PCNA)+ proliferating neural progenitors (Fig. 2A–F). By contrast, somewhat surprisingly, Nat5 expression was considerably more restricted, notably in only a subset of PCNA+ neural progenitors (Fig. 2A–F). Double labelling of Nat5 and Sox1/3 revealed that Nat5+ cells were Sox1/3+ neural progenitors (Fig. 3). Consistent with this, pulse labeling with BrdU revealed that Mdm20+ cells at the VZ were BrdU+ proliferating progenitors (Fig. 4A). Our data also showed that Mdm20+ cells in the mantle

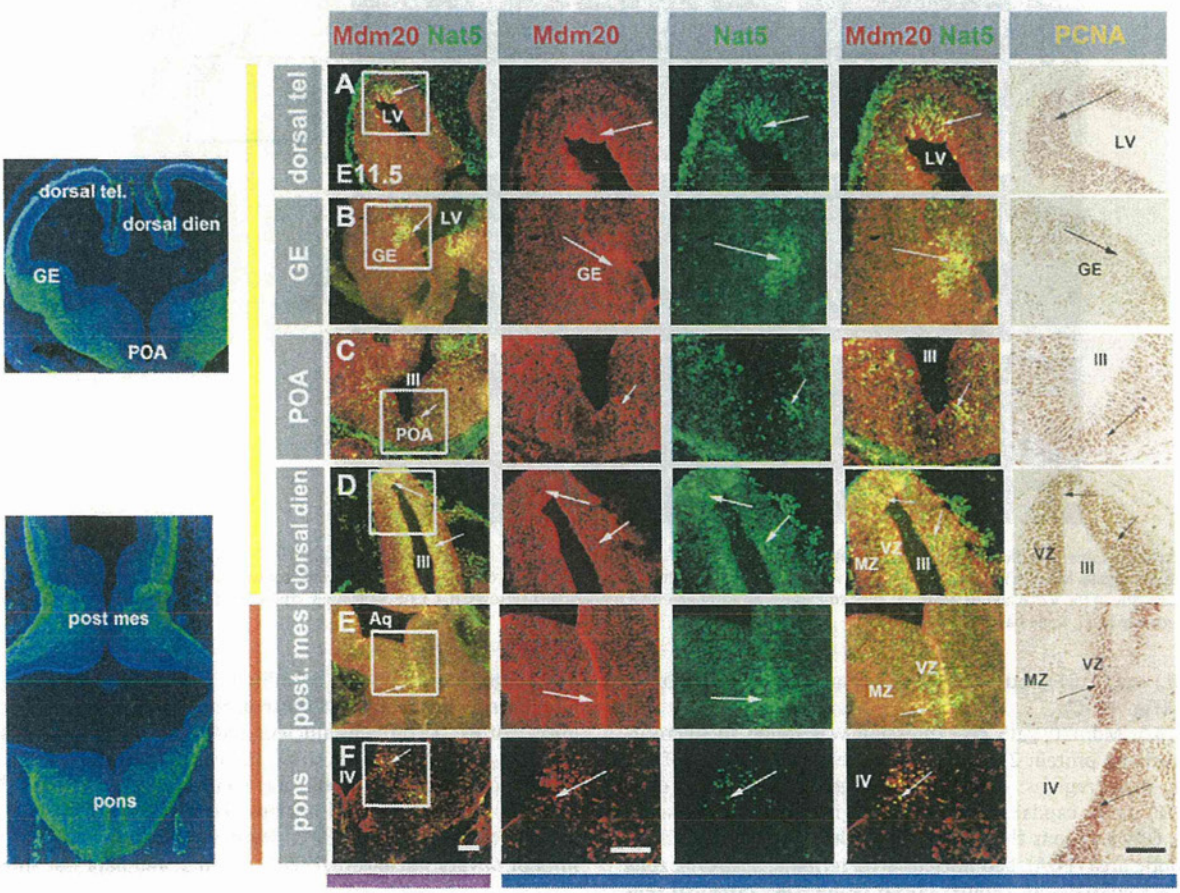

Fig. 2. Expression of Mdm20 and Nat5 in mouse embryonic brain at E11.5. (A–F) Transverse sections through the brain show a widely distributed expression of Mdm20 (red). In contrast, Nat5 expression (green) is restricted to subsets of proliferating cell nuclear antigen (PCNA)+ proliferating neural progenitors at the ventricular zones (VZ) of dorsal telencephalon (tel) (arrows in A), GE and POA in the ventral telencephalon (arrows in B and C), dorsal diencephalon (dien) (arrows in D), posterior mesencephalon (post mes) (arrows in E), and at the border between alar and basal plates of the pons (arrows in F). Nat5 expression was also found in the head mesenchyme. Left panels show TuJ1+ early neurons (green) at lower magnification of the brain tissues with DAPI counter stain (blue). Boxed regions were shown as at higher magnification. PCNA staining was performed at the equivalent levels but in different brain tissues from those for the analysis of Mdm20 and Nat5 expression. LV, lateral venricle; GE, ganglionic eminence; III, the third ventricle; VZ, ventricular zone; MZ, mantle zone; POA, preoprtic area; Aq, aqueduct; IV, the fourth ventricle. Scale bars: 30 μm.

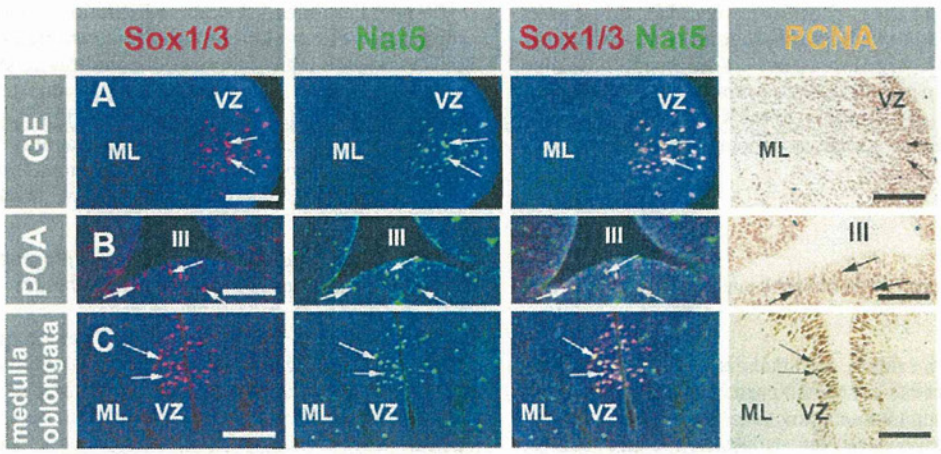

Fig. 3. Nat5 expression in Sox1/3+ neural progenitors at E12.5. (A–C) Transverse sections through the ganglionic eminence (GE), preoptic area (POA), and medulla oblongata at E12.5. Co-expression of Sox1/3 and Nat5 is found in PCNA+ proliferating progenitors at the VZ of the GE, POA, and medulla oblongata (arrows in A–C). GE, ganglionic eminence; POA, preoprtic area; VZ, ventricular zone; ML, mantle layer. III, the third ventricle. Scale bars: 30 μm

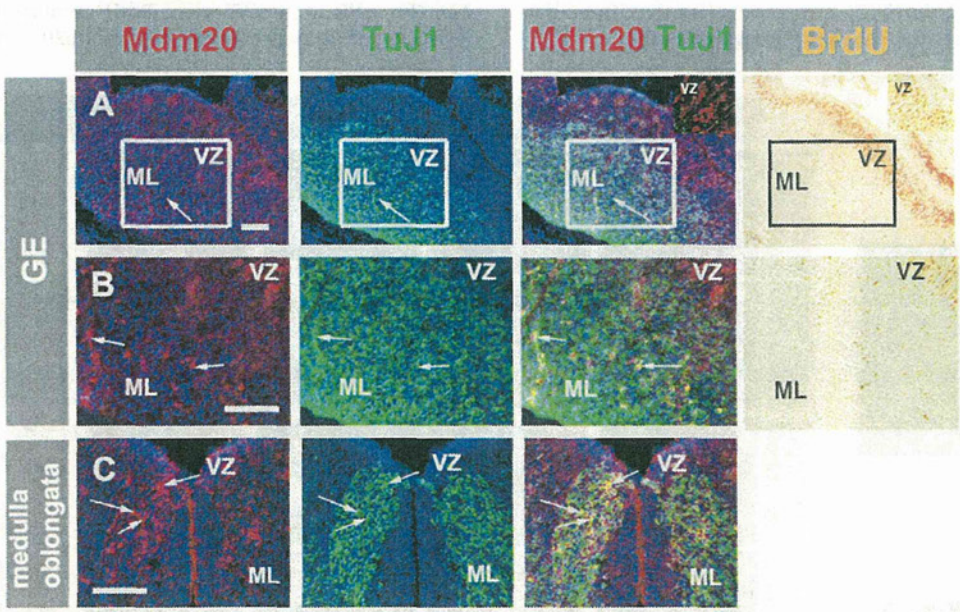

Fig. 4. Mdm20 is expressed in both proliferating neural progenitors at the VZ and TuJ1+ early differentiating neurons at E12.5. (A–C) Transverse sections through the GE and the medulla oblongata. Mdm20 is expressed both in the VZ and ML of both the GE and the medulla oblongata (A–C). Bromodeoxy-uridine (BrdU) pulse-labeled cells for 1hr are located mostly in the VZ (A and B). Mdm20+ cells co-express an early neuronal marker TuJ1 (arrows, A–C). GE, ganglionic eminence; POA, preoprtic area; VZ, ventricular zone; ML, mantle layer. Scale bars: 30 μm.

layer (ML) were TuJ1+, indicating that they are early differentiating neurons (Fig. 4A–C).

By E14.5, Mdm20/Nat5 co-expression was found in microtubule-associated protein 2 (MAP2)+ differentiating neurons of the following brain regions: olfactory bulb, septum, ganglionic eminence (GE) and its caudal part, CGE, which gives rise to amygdaloid neurons. Other regions that co-express Mdm20 and Nat5 include the preoptic area (POA), bed nucleus stria terminalis (BNST), zona incerta (Zi), epithalamus (Epith), dorsal raphe (DR), principal sensory nucleus of trigeminal nerves (Pr5s), vestibular nucleus, cochlear, external cuneate nucleus (EC), medullary raphe (Ra), spinal trigeminal nucleus (Sp5n) and so on (Figs. 5 and 6). It is noteworthy that cerebellar deep neurons express Mdm20 but not Nat5 (Fig. 6E), indicating the existence of Mdm20+/Nat5− cells in the brain.

At E18.5, co-expression of Mdm20/Nat5 was maintained in differentiated neurons such as those in the septum, pineal gland, piriform cortex, accumbens nucleus (NAc), Zi, amygdala, cingulate cortex, ventral tegmental area, interpeduncular nucleus, dorsal raphe, and medullary raphe (Ra) containing serotonergic (5-HT) neurons, spinal trigeminal nucleus (Pr5n), cochlear nucleus, pontine reticular formation (RF), external cuneate nucleus (EC), and inferior olivary nucleus (IO) (Figs. 7 and 9, and data not shown).

1.3. Mdm20 is not necessarily co-expressed with Nat5 in the developing mouse brain

At early stages of neurogenesis (E11.5–12.5), the majority of neural progenitors at the VZ that express Mdm20 do not co-express Nat5 (Fig. 2). Similarly, while a vast majority of Nat5+

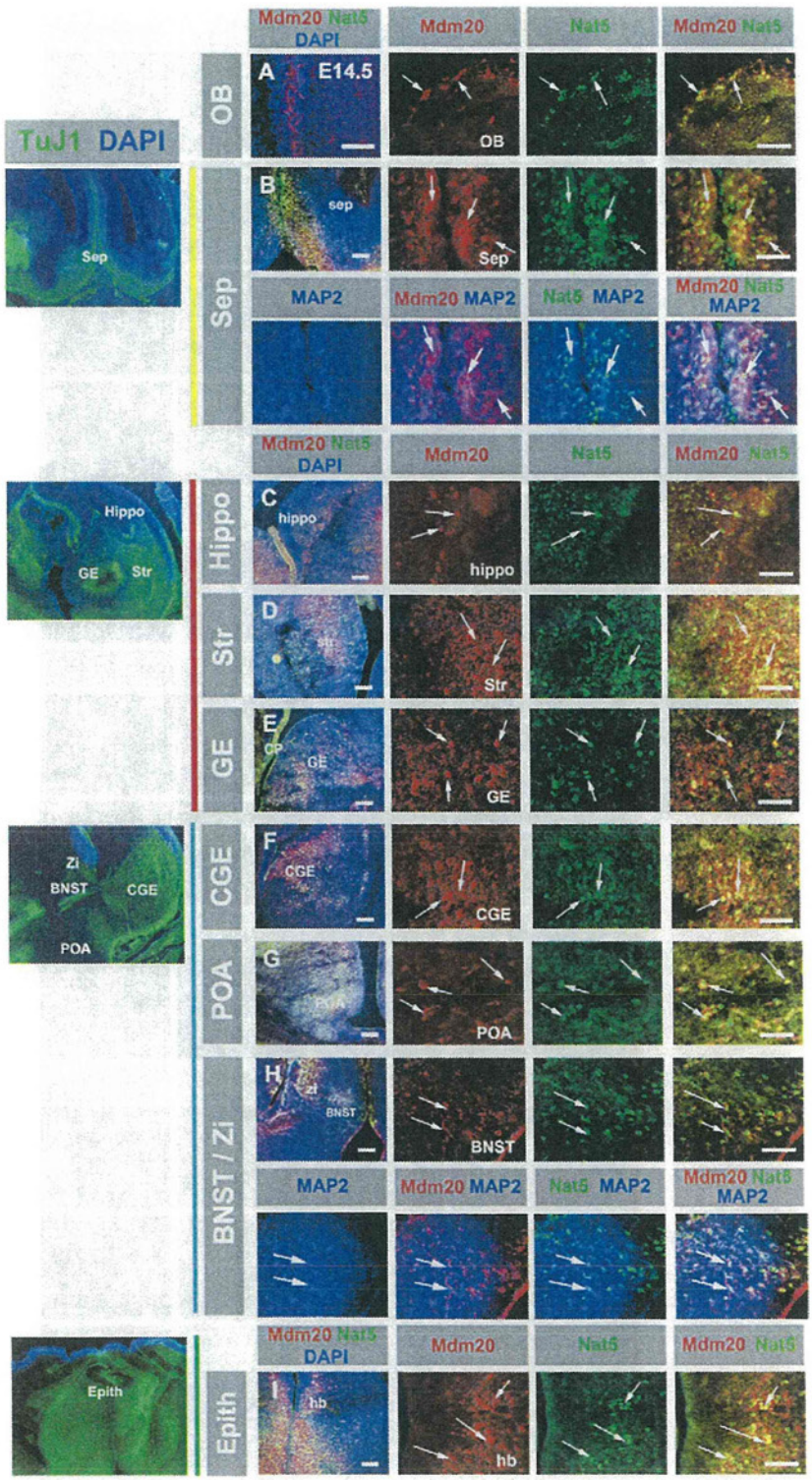

Fig. 5. Expression of Mdm20 and Nat5 in differentiating neurons of mouse embryonic forebrain at E14.5. (A–I) Transverse sections through the mouse forebrain at E14.5. Co-expression of Mdm20 and Nat5 is found in differentiating neurons of the following forebrain regions (arrows) in A–I: (A) olfactory bulb (OB); (B) septum (Sep); (C) hippocampus (Hippo); (D) striatum (Str); (E) ganglionic eminence (GE); (F) caudal ganglionic eminence (CGE); (G) preoptic area (POA); (H) bed nucleus stria terminalis (BNST)/zona incerta (Zi); epithalamus (Epith). Left panels show TuJ1+ early neurons (green) at lower magnification of the brain regions counterstained with DAPI (blue). Co-expression of Mdm20, Nat5, and neuronal marker MAP2 was found in the Sep (arrows in B) and BNST (arrows in H). Scale bars:30 μm on the left column of A–I; 15 μm on the three columns of A-I from the right, showing pictures at a higher magnification.

differentiating neurons co-express Mdm20 at E14.5 and onward, Mdm20+/Nat5− neurons were also observed in the brain regions such as facial nucleus, preoptic area (POA), thalamic paraventricular nucleus (Th PVN), lateral reticular nucleus (LRN), and cerebellar

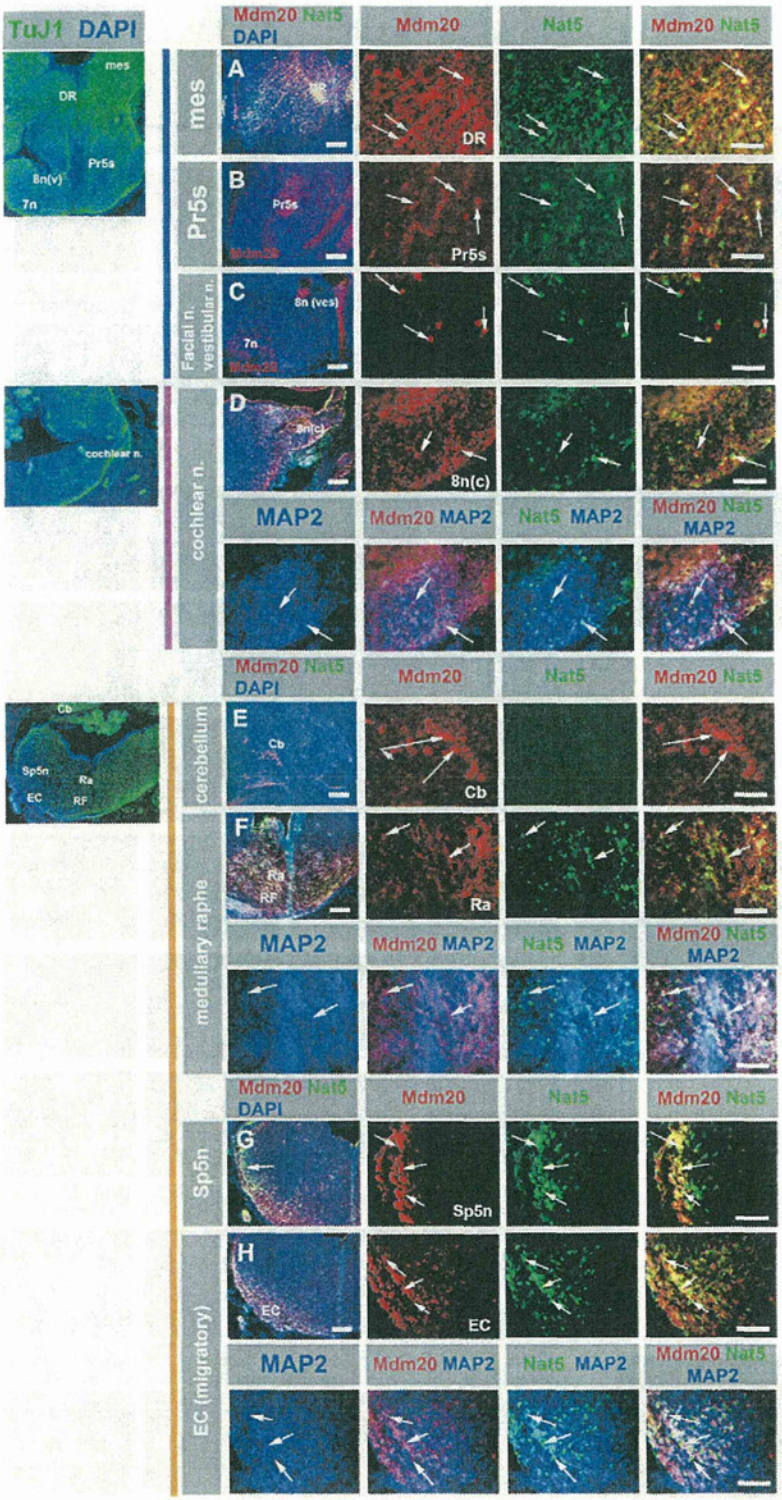

Fig. 6. Mdm20 and Nat5 expression in differentiating neurons of mouse brainstem at E14.5. (A–H) Transverse sections through the mouse brainstem at E14.5. (A–D) Co-expression of Mdm20 (red) and Nat5 (green) in the upper brainstem (arrows): (A) dorsal raphe in the mesencephalon (DR); (B) principal sensory trigeminal nucleus (Pr5s); (C) vestibular nucleus, Note that facial neurons does not express Nat5; (D) cochlear neurons. (E–H) Expression of Mdm20 (red) and Nat5 (green) in the lower brainstem and cerebellum (arrows): (E) cerebellar deep neurons (Cb); (F) medullary raphe neurons (Ra); reticular formation (RF); (G) spinal trigeminal neurons (Sp5n) (arrows); (H) migratory external cuneate neurons (EC) (arrows). Note that cerebellar deep neurons express Mdm20 but not Nat5. Left panels show TuJ1+ early neurons (green) at lower magnification of the brain regions stained wih DAPI (blue). Co-expression of Mdm20, Nat5, and neuronal marker MAP2 was found in the cochlear nucleus (arrows in D), RF (arrows in F), and EC (arrows in H). Scale bars: 30 μm on the left column of A–H; 15 μm on the three columns of A–H from the right, showing pictures at a higher magnification.

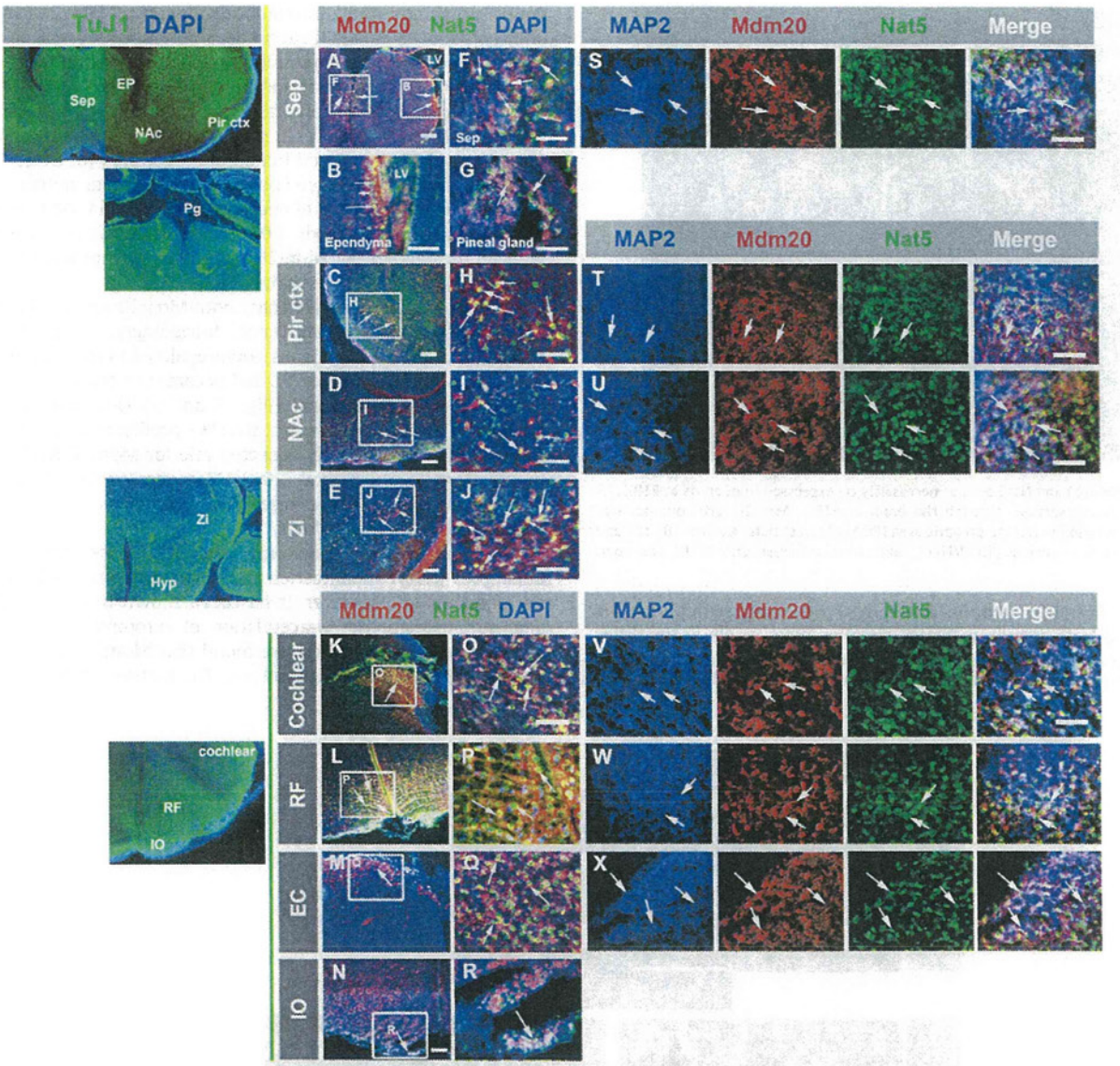

Fig. 7. Mdm20 and Nat5 are co-expressed in differentiated neurons at E18.5. (A–R) Transverse sections through the brain. Co-expression of Mdm20 and Nat5 is found in the septum (arrows in A and F), ependymal cells facing at the lateral ventricle (LV) (arrows in B), piriform cortex (Pir ctx) (arrows in C and H), accumbens nucleus (NAc) (arrows in D and I), zona incerta (Zi) (arrows in E and J), pineal gland (Pg) (arrows in G), cochlear nucleus (arrows in K and O), potine reticular formation (RF) (arrows in L and P), EC (arrows in M and Q), and the ventral portion of inferior olivary nucleus (IO) (arrows in N and R). Left panels show TuJ1+ neurons (green) at a lower magnification of the brain regions stained wih DAPI (blue). hyp; hypothalamus. Co-expression of Mdm20, Nat5, and neuronal marker MAP2 was found in the Sep (arrows in S), Pir ctx (arrows in T), NAc (arrows in U), cochlear nucleus (arrows in V), RF (arrows in W), and EC (arrows in X). Scale bars: 30 μm in A, C, D, E, K–N; 15 μm in B, F-J, O–X.

deep neurons (Figs. 6C and E and 8A–D). Moreover, although vestibular neurons (Ves) co-express Mdm20 and Nat5 at E14, the downregulation of Nat5 occurs in the Ves by E18.5 (Figs. 6C and 8B). These data indicate that the expression of Mdm20 and Nat5 is not only spatially regulated but also changes over time.

Although Mdm20 and Nat5 were found to co-express in the midbrain DA neurons *in vivo* (Fig. 9A–C), we also noted that their subcellular localization appeared to be distinct (Fig. 9A and B). Mdm20 was mainly localized in the cytoplasm, whereas Nat5 was found in the nucleus. This data is consistent with the previous observation using cultured tumor cells (Starheim et al., 2008), although they showed some co-localization of Mdm20 and Nat5 in the cytoplasm. To clarify the subcellular localization of Mdm20 and Nat5 in neurons, we monitored their expression in the midbrain DA neurons cultured *in vitro*. The midbrain was isolated from E18.5 rat embryos and cultured for 2–4 weeks. Expression of Mdm20 and Nat5 was assessed by an immunofluorescent labeling experiment. Consistent with *in vivo* data (Fig. 9A–C), Mdm20 was mainly localized in the cytoplasm especially in the perinuclear region of tyrosine hydroxylase (TH)+ DA neurons, whereas Nat5 was mainly in the nucleus (Fig. 9D–G).

2. Discussion

In the present study, we have documented the spatial and temporal expression pattern of Mdm20 in comparison with that of Nat5 in the developing mouse brain. Mdm20 is highly expressed in the developing mouse brain. Early on, it is widely distributed in neural progenitors (Figs. 1–4). As development proceeds, Mdm20 expression is downregulated in proliferating progenitors and found in differentiating neurons (Figs. 5–7). The vast majority

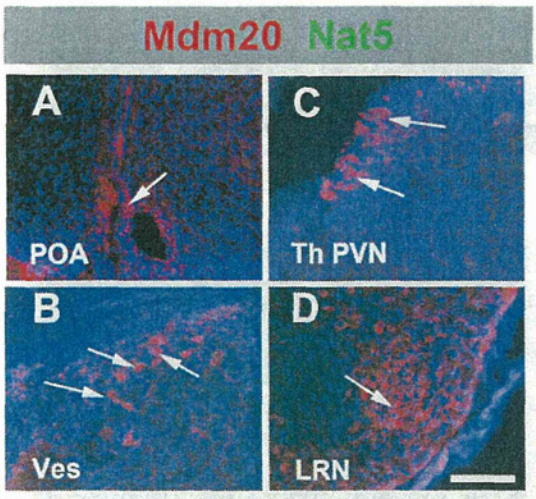

Fig. 8. Mdm20 and Nat5 are not necessarily co-expressed in neurons at E18.5. (A–D) Transverse sections through the brain at E18.5. Mdm20 (red) but not Nat5 (green) is found in (A) the preoptic area (POA) (A), vestibular nucleus (B), thalamic paraventricular nucleus (Th PVN) (C), and lateral reticular nucleus (D). Scale bars: 30 μm.

of the Mdm20+ neurons co-express Nat5, suggesting that the Mdm20/Nat5 acetyltransferase complex plays a role in the differentiation of neurons. Careful analysis of the expression pattern of Mdm20 and Nat5 also reveals the existence of Mdm20+/Nat5– neural progenitors and differentiating neurons (Figs. 2 and 8), and their subcellular localization does not entirely overlap in differentiated neurons as seen in midbrain DA neurons (Fig. 9).

Previous studies of yeast and human cells *in vitro* showed that Mdm20 controls cell proliferation and actin dynamics (Singer and Shaw, 2003; Starheim et al., 2008). Consistent with this notion, Mdm20 is widely expressed in neural progenitors (at E11.5–12.5) (Figs. 1 and 2). Given that cell polarity of neural progenitors is crucial to control the number of neural progenitors and their differentiation (Huttner and Kosodo, 2005), further studies are needed to explore the function of Mdm20 in proliferating progenitors and their differentiation in the brain.

Our data has also revealed that both Mdm20 and Nat5 expression changes in space and time. Intriguingly, by E14.5, both Mdm20 and Nat5 expression is downregulated in most of the proliferating progenitors at the VZ and becomes restricted to postmitotic differentiating neurons (Figs. 5 and 6). Our observation of Nat5/Mdm20 co-expression in Sox1/3+ proliferating neural progenitors supports a widely accepted role for Mdm20/Nat5 in cell proliferation (Starheim et al., 2008). Moreover, our data imply that Mdm20/Nat5 has an unidentified additional role in differentiating neurons as we discuss below.

Biochemical studies previously showed that serotonin (5-HT) undergoes acetyl modification and conversion to melatonin in the pineal gland. However, it has been shown that Nat1/NATH1 does not mediate the *N*-acetylation of serotonin (Heim et al., 1991). In the present study, we found that Mdm20 and Nat5 are co-expressed in the pineal gland (Fig. 7G). It raises a possibility that

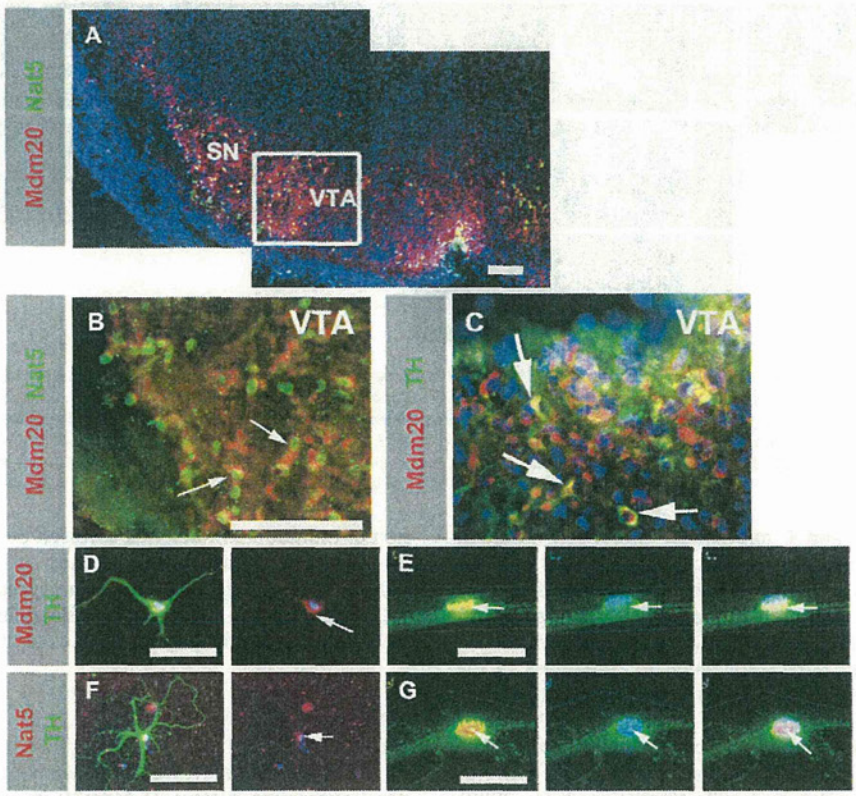

Fig. 9. Subcellular localization of Mdm20 and Nat5 protein in midbrain DA neurons. (A–C) Mdm20 (red) and Nat5 (green) are co-expressed in tyrosine hydroxylase (TH)+ dopaminergic (DA) neurons at the substantia nigra (SN) and the ventral tegmental area (VTA) in mouse midbrain (arrows). (D–I) Subcellular localization of Mdm20 (red) and Nat5 (red) in the rat midbrain DA neurons (green) cultured *in vitro*. To clarify the subcellular localization of both Mdm20 and Nat5, cell nuclei were visualized by DAPI staining (blue in E and G). Mdm20 (red) is mainly localized in the cytoplasm especially in the perinuclear region of the TH + DA neurons (arrows in D and E; note that Mdm20 is localized at the vicinity of DAPI+ cell nucleus), whereas Nat5 (red) is in the nucleus (arrows in F and G; note that Nat5 expression is overlapped with DAPI+ cell nucleus). Scale bars: 30μm in A–D, F; 5 μm in E and G.